Title
Aspects of Density Wave States and Quantum Phase Transitions

Author
Powell, Ian Emmanuel

Publication Date
2021

Peer reviewed|Thesis/dissertation

UNIVERSITY OF CALIFORNIA

Los Angeles

Aspects of Density Wave States and Quantum Phase Transitions

A dissertation submitted in partial satisfaction

of the requirements for the degree

Doctor of Philosophy in Physics

by

Ian Emmanuel Powell

2021

ABSTRACT OF THE DISSERTATION

Aspects of Density Wave States and Quantum Phase Transitions

by

Ian Emmanuel Powell
Doctor of Philosophy in Physics
University of California, Los Angeles, 2021
Professor Sudip Chakravarty, Chair

In chapter 2 we offer a pedagogic introduction to quantum phase transitions and quantum critical behavior in scalar ϕ^4 theory. We focus on characterizing the quantum critical fan, and we explicitly show how one can identify the borders of said fan using the familiar arguments introduced by S. Chakravarty, B. I. Halperin, and D. R. Nelson[CHN89] in 1989. By calculating the renormalization group flow equations to one loop we are able to approximately calculate the correlation lengths in the theory, and from the behavior of the obtained correlation length we are then able to identify the phases of our theory as ordered, quantum critical, or quantum disordered.

In chapter 3 we investigate the effect that density wave states have on the Hofstadter Butterfly. We first review the problem of the d-density wave on a square lattice and then numerically solve the d-density wave problem when an external magnetic field is introduced. As the d-density wave condensation strength is tuned the spectrum evolves through three topologically distinct butterflies, and a relativistic quantum Hall effect is observed. The chiral $p + ip$-density wave state demonstrates drastically different Hofstadter physics–inducing a destruction of the gaps in the butterfly which causes electrons' cyclotron orbits to not obey any type of Landau quantization, and the creation of a large gap in the spectrum with Hall conductance σ_{xy}=0. To investigate the quantum phases in the system we perform a multifractal analysis of the single particle wavefunctions. We find that tuning the d-

density wave strength at a generic value of magnetic flux controls a metal-metal transition at charge neutrality where the wavefunction multifractality occurs at energy level crossings. In the $p + ip$ case we observe another metal-metal transition occurring at an energy level crossing separated by a strongly multifractal quasi-insulating island state occurring at charge neutrality and strip dimerization of the lattice.

In chapter 4 we discuss recent anomalous transport measurements that have been observed through a wide doping range in the cuprates. We investigate the effects of a state that shares many features consistent with those of the pseudogap, the mixed triplet-singlet d-density wave state, and examine whether its presence could help explain these observations. For a sufficiently doped system Li & Lee [arXiv:1905.04248v3] showed that that these density wave states produce a nonzero thermal Hall effect. Through the effect that density waves have on the localized spins of a square lattice in a magnetically ordered phase, we find that the mixed triplet-singlet d-density wave state induces *stable* Dzyaloshinskii-Moriya (DM) interactions among the localized spins in the presence of an external magnetic field. As similar antisymmetric exchange couplings have yielded nonzero thermal Hall contributions, we examine this induced DM interaction by applying Holstein–Primakoff (HP) transformations to study the resulting magnon excitations of the spin models for both antiferromagnetic and ferromagnetic backgrounds–relevant to the near-half-filling and heavily overdoped regimes respectively. Furthermore, because the triplet-singlet d-density wave is experimentally challenging to detect directly, we discuss the magnetic signatures that this state can possibly induce away from the pseudogap regime. We calculate the magnon dispersion for $La_{2-x}Sr_xCuO_4$ (LSCO) and find that the density wave induces a weak $d_{x^2-y^2}$ anisotropy; upon calculating the non-abelian Berry curvature for this magnon branch, we show explicitly that the magnon contribution to κ_{xy} is zero. Finally, we calculate corrections to the magnetic ground state energy, spin canting angles, and the spin-wave dispersion due to the topological density wave for ferromagnetic backgrounds. We find that terms *linear* in the HP bosons can affect the critical behavior, a point previously overlooked in the literature.

The dissertation of Ian Emmanuel Powell is approved.

Yaroslav Tserkovnyak

Stuart Brown

Per Kraus

Sudip Chakravarty, Committee Chair

University of California, Los Angeles

2021

To my dear family and friends

TABLE OF CONTENTS

LIST OF FIGURES

VITA

2015	B.S. (Physics) with minor (Mathematics), California Polytechnic State University.
2017	M.S. (Physics), UCLA, Los Angeles, California.
2015–2021	Teaching Assistant, Department of Physics and Astronomy, UCLA.

PUBLICATIONS

Powell, I. E., Durr, S., Rombes, N. and Chakravarty, S. *Density Wave Mediated Dzyaloshinskii Moriya Interactions.*, Phys. Rev. B. **103**(2):024433, January 2021

Powell, I. E., and Chakravarty, S. "Density Wave States in the Presence of an External Magnetic Field." Phys. Rev. B, **100**(7):075150, 27, August 2019

Powell, I. E., & Chakravarty, S. Characterizing the Quantum Critical Fan in ϕ^4 Theory, *in preparation*

CHAPTER 1

Introduction

With the development of quantum mechanics in the early 20th century came a flurry of exciting, new ideas related to the implications of its predictions. One of these ideas was that of a quantum phase transition. Classically it is understood that a phase transition is driven by the competition between the energy of a system and the entropy of its thermal fluctuations. The critical point–i.e. the temperature, pressure, etc. at which the system undergoes a phase transition, demarcates phases from one another and is signified as the location of a cusp (singularity of a derivative) in the free energy. Given this classical notion of a phase transition, and given the fact that the entropy of an isolated system at zero temperature must also be zero, phase transitions at zero temperature could never occur. Quantum mechanical fluctuations, on the other hand, offered a new mechanism by which phase transitions may occur at zero temperature.

In the seminal work by S. Chakravarty, B. I. Halperin, and D. R. Nelson [CHN89] the low energy properties of the two-dimensional quantum Heisenberg antiferromagnet were analyzed in detail via a mapping of the problem to that of the non-linear sigma model in 2+1 dimensions. By categorizing the system in terms of the behavior of the correlation length in the physical coupling space the authors were able to identify the phases of the model: ordered, renormalized classical, quantum disordered, and quantum critical. The quantum critical regime being a relatively large portion of the coupling space in which the system's behavior is entirely dictated by the zero-temperature quantum critical point. This quantum critical regime displays interesting, and unusual behavior–from a correlation length that decays away from the critical point algebraically in its temperature dependence, to gapless excitations. In chapter 2 we offer a pedagogic introduction to characterizing the

quantum critical fan for a ϕ^4 theory of the Ising universaltiy class. By working through similar arguments we offer some foundation to understand the peculiar physics emanating from the quantum critical point into a finite region of temperature.

Another fascination of the 20th century is the Hofstadter butterfly. When electrons in two dimensions are subjected to both a periodic potential of a crystalline lattice and a uniform magnetic field the two competing length scales, that of the Landau cyclotron orbits and that of the crystalline lattice, give rise to quantum fractal spectra–"Hofstadter's butterfly." This system has provided an interesting basis for much research over the years. The effects of mutual Coulomb interactions in GaAs[GG96] and Graphene[AC14],[LC15]have been considered, as well as disorder[ABA05], impurity effects[PG92], and much more. Despite the beauty and the complexity of the structure it has remained somewhat elusive because these length scales are typically severely mismatched. Advances in experimentally measuring the fractal energy spectrum in GaAs heterostructures[ASK01],[MBZ04] as well as in the moiré superlattice of bilayer graphene [YJ18] have opened up the possibility of investigating emergent behavior within a fractal landscape. In chapter 3 we investigate a certain family of models in this landscape that we will discuss in what follows.

The cuprate phase diagram (shown in Fig. 1.1), namely the so-called "pseudogap" phase, found to the left of the line marked T^* in Figure 1.1 has perplexed physicists for decades. It is so far unclear which of a variety of order parameters is responsible for the development of the gap in this phase. Promising candidates are the family of d-density wave (DDW) orders–namely the singlet and triplet versions previously proposed[CLM01] to potentially develop in the pseudogap phase. These density waves are the generalizations of charge and spin density waves to higher angular momentum channels. A general density wave state is comprised of a particle-hole condensate (in a similar spirit to that of the BCS state which can be visualized as a particle-particle condensate), and, in the d angular momentum channel, can be visualized as an alternating charge (singlet DDW) or spin (triplet DDW) currents on the bonds of the square lattice. In Chapter 3 we investigate these d-density waves, and chiral $p + ip$ density waves, in the fractal landscape of the Hofstadter butterfly–focusing on

characterizing the various quantum phase transitions that take place.

In Chapter 4 we discuss the relevance of a certain "hidden" DDW order, the topological triplet-singlet DDW, to results obtained in a recent experiment [GLB19] that showed an anomalous thermal Hall conductance for a variety of doping strengths in multiple cuprate compounds. Recently Z.X. Li and D. H. Lee have shown that this topological variant of the d-density wave produces a nonzero thermal Hall conductance [LL19] in the pseudogap regime of doping, and Samajdar, Scheurer et al. have shown that there can be spin-wave contributions to the thermal Hall effect [SCS19]. With these results in mind, we investigate the effects that this topological variant of the d-density wave can have on an underlying spin system (both ferromagnetic and antiferromagnetic for the heavily overdoped and underdoped case respectively), and show that it produces an effective Dzyaloshinskii-Moriya interaction. We show that the magnon excitations of the resulting effective magnetic Hamiltonian *can not* contribute to the thermal Hall effect, which is consistent with speculations on the nature of the excitations responsible for the signal. The signatures that a triplet d-density wave leaves on the underlying spin system could be used to detect the presence of such a hidden order, which is not detectable using typical experimental probes such as neutron scattering, and thus assess its relevance to the pseudogap phase of the cuprates.

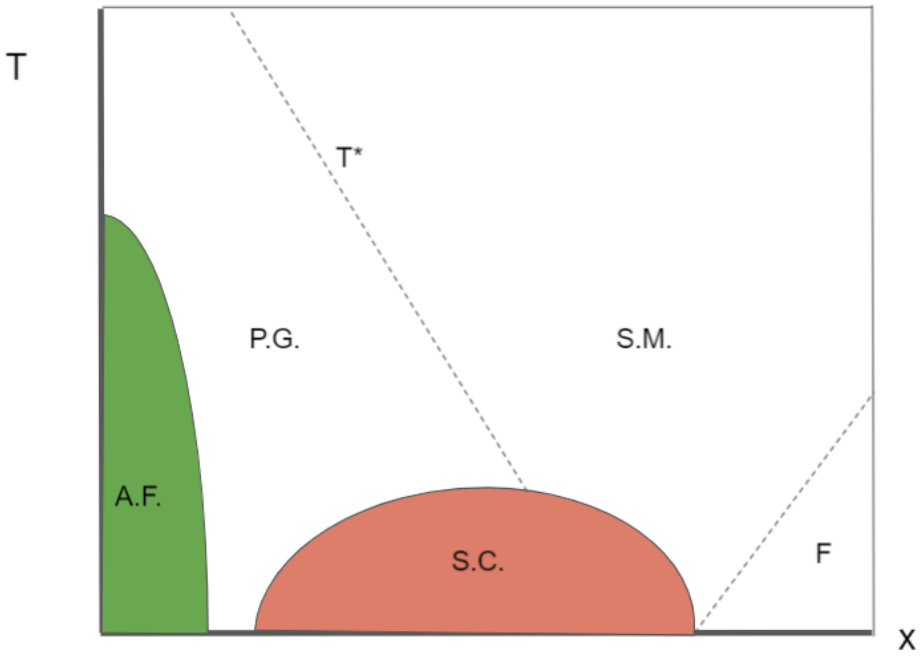

Figure 1.1: Simplified phase diagram of the high T_c cuprate superconductors plotted against the temperature, T, and hole doping, x. At sufficiently low temperature, and low doping, the material is in its Mott insulating antiferromagnetic phase (A.F.). Increasing the doping brings us to the enigmatic pseudogap phase (P.G.) where the Fermi surface has characteristic hole pockets on the diagonals in the Brillouin zone[CLM01]. T^* demarcates the pseudogap phase from the strange metal (S.M) phase where the resistivity is linear in temperature, and the physics is consistent with that of a quantum critical regime emanating from a quantum critical point obfuscated by the superconducting (S.C.) dome. In the underdoped regime there are a host of other competing orders, such as stripe, checkerboard charge order, and spin glass order. In the highly overdoped regime it was recently conjectured [KGC07] and experimentally confirmed that the cuprates develop Ferromagnetic order (F).

CHAPTER 2

Characterizing the Quantum Critical Fan of a ϕ^4 Theory

2.1 Introduction

This chapter is meant to serve as an introduction to quantum criticality in many body systems with a particular emphasis on characterizing what is known as the quantum critical fan. The quantum critical fan is the finite-temperature region in which the physics of the system is governed by the zero temperature quantum critical point that demarcates quantum phases from one another. We focus on characterizing the quantum critical fan, and we explicitly show how one can identify the borders of said fan using the arguments introduced by S. Chakravarty, B. I. Halperin, and D. R. Nelson (CHN) in 1989[CHN89]. In their work, CHN categorized the phases of the two dimensional non-linear sigma model in $d = 2 + 1$ dimensions by the behavior of the correlation length which is yielded via a 1-loop RG approach. In this chapter we utilize and discuss these tools developed by CHN in the familiar setting that is ϕ^4 theory in hopes of providing a pedagogic introduction to characterizing quantum critical fans.

We begin by reviewing the calculation of the renormalization group flow equations to one loop for the couplings and dimensionless temperature for the one component ϕ^4 theory of the Ising universality class in d+1 space-time dimensions. Working in a convenient dimension we then identify the quantum critical fan, and characterize the rest of the parameter space

as either quantum disorded, or ordered in accordance with the behavior of the correlation length.

2.2 The mass RG Equation

The Euclidean action we investigate is

$$S[\phi] = \int d^d x \int_0^\beta d\tau \frac{1}{2}\left((\nabla\phi)^2 + (\partial_\tau \phi)^2\right) + \frac{1}{2}m_0^2\phi^2 + \frac{\lambda_0}{4!}\phi^4, \tag{2.1}$$

where we are working in units where $\hbar = k_B = 1$. This action can be understood as arising from either of two equivalent models: (1) this action can be interpreted as that of an classical Ising model in $d+1$ dimensions where the imaginary temporal dimension corresponds to a compactified spatial dimension which is periodic in β, with the mass variable, m_0^2, functioning as a reduced temperature; (2) this action can be understood as that which corresponds to a quantum Ising model in d dimensions[Sac11] where m_0^2 controls a quantum phase transition from an Ising ferromagnet to a quantum disordered state. From the point of view of (1), going from Ising variables to this field theory in the auxiliary variable, ϕ, is typically achieved by utilizing a Hubbard Stratonovich substitution, and then dropping higher order terms $O(\phi^6)$ and above. In the following we will step away from the classical Ising interpretation of this action, and instead associate the mass m_0^2 as the variable which delineates ordered and disordered quantum phases depending on its sign. Going to momentum space we Fourier/Matsubara expand the fields

$$\phi = \sum_{n=-\infty}^{\infty} \int \frac{d^d\vec{k}}{(2\pi)^d} \tilde{\phi}(\vec{k}, \omega_n) e^{i(\vec{k}\cdot x - \omega_n t)}, \tag{2.2}$$

where $\omega_n = (2\pi n)/\beta$. Integrating out position and imaginary time we yield

$$S[\tilde{\phi}] = S_0[\tilde{\phi}] + S_{int}[\tilde{\phi}], \tag{2.3}$$

where

$$S_0[\tilde{\phi}] = \sum_{n=-\infty}^{\infty} \int \frac{d^d\vec{k}}{(2\pi)^d} \frac{\beta}{2} \tilde{\phi}(\vec{k}, \omega_n)(\vec{k}^2 + \omega_n^2 + m_0^2)\tilde{\phi}^*(\vec{k}, \omega_n), \tag{2.4}$$

and

$$S_{int}[\phi] = \frac{\lambda_0 \beta}{4!} \sum_{n_1,n_2,n_3=-\infty}^{\infty} \int \frac{d^d\vec{k_1}}{(2\pi)^d} \frac{d^d\vec{k_2}}{(2\pi)^d} \frac{d^d\vec{k_3}}{(2\pi)^d} \tilde{\phi}(\vec{k_1}, \omega_{n_1}) \tilde{\phi}(\vec{k_2}, \omega_{n_2}) \tilde{\phi}(\vec{k_3}, \omega_{n_3}) \tilde{\phi}(\vec{k_4}, \omega_{n_4}), \quad (2.5)$$

where $\vec{k_4} = -(\vec{k_1} + \vec{k_2} + \vec{k_3})$, $n_4 = -(n_1 + n_2 + n_3)$, and we integrate the momenta up to a cutoff Λ.

We can read the propagator directly from the free part of the Lagrangian as

$$\langle \tilde{\phi}^*(\vec{k}, \omega_n) \tilde{\phi}(\vec{k'}, \omega_m) \rangle = \frac{1}{\beta} \frac{(2\pi)^d \delta(\vec{k} + \vec{k'}) \delta_{n+m}}{\vec{k}^2 + \omega_n^2 + m_0^2}. \quad (2.6)$$

To yield the RG equations we follow the Wilsonian method of systematically integrating out the high momentum modes and rescaling our system. The interval which we integrate out is $b\Lambda < |\vec{k}| < \Lambda$, where $0 < b < 1$. We thus divide our field into high and low momenta components

$$\tilde{\phi}(\vec{k}, \omega_n) = \Theta(\vec{k} - b\Lambda) \tilde{\phi_H}(\vec{k}, \omega_n) + \Theta(-\vec{k} + b\Lambda) \tilde{\phi_L}(\vec{k}, \omega_n). \quad (2.7)$$

Substituting this expression into our action yields

$$S[\tilde{\phi}] = S_L[\tilde{\phi}_L] + S_H^0[\tilde{\phi}_H] + S_{int}[\tilde{\phi}_L, \tilde{\phi}_H], \quad (2.8)$$

where

$$S_L[\tilde{\phi}_L] = \sum_{n=-\infty}^{\infty} \int_0^{b\Lambda} \frac{d^d\vec{k}}{(2\pi)^d} \frac{\beta}{2} \tilde{\phi_L}(\vec{k}, \omega_n)(\vec{k}^2 + \omega_n^2 + m_0^2) \tilde{\phi_L}^*(\vec{k}, \omega_n)$$
$$+ \frac{\lambda_0 \beta}{4!} \sum_{n_1,n_2,n_3=-\infty}^{\infty} \int_0^{b\Lambda} \frac{d^d\vec{k_1}}{(2\pi)^d} \frac{d^d\vec{k_2}}{(2\pi)^d} \frac{d^d\vec{k_3}}{(2\pi)^d} \tilde{\phi_L}(\vec{k_1}, \omega_{n_1}) \tilde{\phi_L}(\vec{k_2}, \omega_{n_2}) \tilde{\phi_L}(\vec{k_3}, \omega_{n_3}) \tilde{\phi_L}(\vec{k_4}, \omega_{n_4}), \quad (2.9)$$

$$S_H^0[\tilde{\phi}_H] = \sum_{n=-\infty}^{\infty} \int_{b\Lambda}^{\Lambda} \frac{d^d\vec{k}}{(2\pi)^d} \frac{\beta}{2} \tilde{\phi_H}(\vec{k}, \omega_n)(\vec{k}^2 + \omega_n^2 + m_0^2) \tilde{\phi_H}^*(\vec{k}, \omega_n), \quad (2.10)$$

and

$$S_{int}[\tilde{\phi}_L, \tilde{\phi}_H] = \frac{\lambda_0 \beta}{4!} \sum_{n_1,n_2,n_3=-\infty}^{\infty} \int \frac{d^d\vec{k_1}}{(2\pi)^d} \frac{d^d\vec{k_2}}{(2\pi)^d} \frac{d^d\vec{k_3}}{(2\pi)^d} \left[\tilde{\phi_H}^4 + \tilde{\phi_L} \tilde{\phi_L} \tilde{\phi_H} \tilde{\phi_H} + ... \right], \quad (2.11)$$

where the ... corresponds to all possible permutations of terms bilinear in both of the low and high fields. It is implied that the momentum and Matsubara frequency number associated with each field corresponds to its position in the expression.

The partition function for the theory is rewritten as

$$Z = \int D\tilde{\phi} e^{-S[\tilde{\phi}]} = \int D\tilde{\phi_L} D\tilde{\phi_H} e^{-S_L[\tilde{\phi}_L]} e^{-S_H^0[\tilde{\phi}_H]} e^{-S_{int}[\tilde{\phi}_L, \tilde{\phi}_H]}. \tag{2.12}$$

All of the math done above has been motivated by the finding of our effective theory at low energies which is governed by the Boltzmann factor

$$e^{-S_{\text{eff}}[\tilde{\phi}_L]} = e^{-S_L[\tilde{\phi}_L]} \int D\tilde{\phi_H} e^{-S_H^0[\tilde{\phi}_H]} e^{-S_{int}[\tilde{\phi}_L, \tilde{\phi}_H]} = e^{-S_L[\tilde{\phi}_L]} \langle e^{-S_{int}[\tilde{\phi}_L, \tilde{\phi}_H]} \rangle_H. \tag{2.13}$$

We must solve this problem perturbatively so we perform a cumulant expansion on the interacting term

$$\langle e^{-S_{int}} \rangle = e^{-\langle S_{int} \rangle + 1/2(\langle S_{int}^2 \rangle - \langle S_{int} \rangle^2) + \cdots}. \tag{2.14}$$

Going to one loop we must calculate the terms $\langle S_{int} \rangle_H$ and $\langle S_{int}^2 \rangle_H$. This amounts to calculating the diagrams in Fig. 2.1, where the external legs have low momenta and the loops have high momenta. One should also notice that terms of the form $\langle S_{int} \rangle^2$ do not contribute to renormalizing our couplings because they do not represent one particle irreducible graphs.

We first calculate the self energy diagrams that couple to the low momenta fields.

$$\langle S_{int} \rangle_H = \frac{\lambda_0 \beta}{4!} \sum_{n_1, n_2, n_3 = -\infty}^{\infty} \int \frac{d^d \vec{k_1}}{(2\pi)^d} \frac{d^d \vec{k_2}}{(2\pi)^d} \frac{d^d \vec{k_3}}{(2\pi)^d} \left[\tilde{\phi_L} \tilde{\phi_L} \langle \tilde{\phi_H} \tilde{\phi_H} \rangle_H + ... \right], \tag{2.15}$$

Because of the symmetry of the fields in their momentum arguments we can just rewrite this as

$$\langle S_{int} \rangle_H = \frac{\lambda_0 \beta}{4} \sum_{n_1, n_2, n_3 = -\infty}^{\infty} \int \frac{d^d \vec{k_1}}{(2\pi)^d} \frac{d^d \vec{k_2}}{(2\pi)^d} \frac{d^d \vec{k_3}}{(2\pi)^d} \left[\tilde{\phi_L} \tilde{\phi_L} \langle \tilde{\phi_H} \tilde{\phi_H} \rangle_H \right], \tag{2.16}$$

because there are six terms bilinear in the low and high momenta fields. Using Eq. 2.6 we write

$$\langle \tilde{\phi}_H^*(\vec{k}, \omega_n) \tilde{\phi}_H(\vec{k'}, \omega_m) \rangle_H = \frac{1}{\beta} \frac{(2\pi)^d \delta(\vec{k} + \vec{k'}) \delta_{n+m}}{\vec{k}^2 + \omega_n^2 + m_0^2}, \tag{2.17}$$

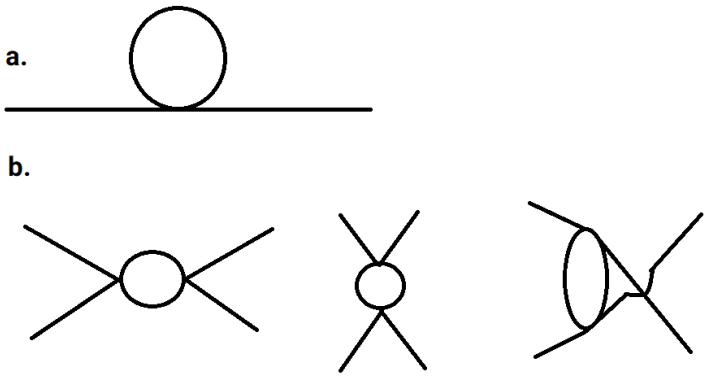

Figure 2.1: Feynmann diagrams associated with the terms generated in the cumulant expansion.

which, upon substitution into Eq. 2.16, yields

$$\langle S_{int}\rangle_H = \frac{\lambda_0}{4}\sum_{n_1,n_2,n_3=-\infty}^{\infty}\int_{\text{low}}\int_{\text{low}}\int_{\text{high}}\frac{d^d\vec{k_1}}{(2\pi)^d}\frac{d^d\vec{k_2}}{(2\pi)^d}\frac{d^d\vec{k_3}}{(2\pi)^d}\left[\tilde{\phi}_L\tilde{\phi}_L\frac{(2\pi)^d\delta(-\vec{k_1}-\vec{k_2})\delta_{n_1+n_2}}{\vec{k_3}^2+\omega_{n_3}^2+m_0^2}\right]. \tag{2.18}$$

Integrating over the Dirac delta functions and summing over the Kronecker-delta gives us

$$\langle S_{int}\rangle_H = \frac{\lambda_0}{4}\sum_{n=-\infty}^{\infty}\int_{\Lambda b}^{\Lambda}\frac{d^d\vec{p}}{(2\pi)^d}\frac{1}{|\vec{p}|^2+(2\pi n/\beta)^2+m_0^2}\sum_{m=-\infty}^{\infty}\int_0^{\Lambda b}\frac{d^d\vec{k}}{(2\pi)^d}|\tilde{\phi}_L(\vec{k},\omega_m)|^2. \tag{2.19}$$

We make use of the fact that

$$\sum_{n=-\infty}^{\infty}\frac{1}{|\vec{p}|^2+(2\pi n/\beta)^2+m_0^2}=\frac{\beta}{2\sqrt{|\vec{p}|^2+m_0^2}}\coth\left[\frac{\beta}{2}\sqrt{|\vec{p}|^2+m_0^2}\right], \tag{2.20}$$

to perform the summation in equation 2.19 resulting in

$$\langle S_{int}\rangle_H = \frac{\lambda_0}{4}\int_{\Lambda b}^{\Lambda}\frac{d^d\vec{p}}{(2\pi)^d}\frac{\beta}{2\sqrt{|\vec{p}|^2+m_0^2}}\coth\left[\frac{\beta}{2}\sqrt{|\vec{p}|^2+m_0^2}\right]\sum_{m=-\infty}^{\infty}\int_0^{\Lambda b}\frac{d^d\vec{k}}{(2\pi)^d}|\tilde{\phi}_L(\vec{k},\omega_m)|^2. \tag{2.21}$$

Because this expression is bilinear in the low momenta fields we add this pre-factor to the bare mass to yield the renormalized mass in the effective theory. In other words

$$m^2 = m_0^2+\frac{\lambda_0}{4}\int_{\Lambda b}^{\Lambda}\frac{d^d\vec{p}}{(2\pi)^d}\frac{1}{\sqrt{|\vec{p}|^2+m_0^2}}\coth\left[\frac{\beta}{2}\sqrt{|\vec{p}|^2+m_0^2}\right] \tag{2.22}$$

to one loop. We now define $b = e^{-l}$, rescale the couplings, and differentiate Eq. 2.22 to yield the RG flow. Rescaling the couplings amounts to nondimensionalizing them according to our new cutoff $b\Lambda$. Thus

$$m^2(l) = \tilde{m}^2\Lambda^2 e^{-2l}, \tag{2.23}$$

$$\lambda(l) = \tilde{\lambda}\Lambda^{(3-d)}e^{-(3-d)l}, \tag{2.24}$$

$$\beta(l) = u\Lambda^{-1}e^{l}, \tag{2.25}$$

where the tilde denotes a coupling being dimensionless. After nondimensionalizing our couplings we write Eq. 2.22 as

$$\tilde{m}^2\Lambda^2 e^{-2l} = \Lambda^2 \tilde{m_0}^2 + \frac{\tilde{\lambda_0}\Lambda^{(3-d)}}{4}\int_{\Lambda e^{-l}}^{\Lambda}\frac{d^d\vec{p}}{(2\pi)^d}\frac{1}{\sqrt{|\vec{p}|^2+m_0^2}}\coth\left[\frac{\beta}{2}\sqrt{|\vec{p}|^2+{m_0}^2}\right]. \tag{2.26}$$

The momentum integration is performed over the d-dimensional hypersphere. We perform d-1 angular integrations and yield

$$\tilde{m}^2\Lambda^2 e^{-2l} = \tilde{m_0}^2\Lambda^2 + \frac{\tilde{\lambda_0}\Lambda^{(3-d)}}{4}\int_{\Lambda e^{-l}}^{\Lambda} dp\frac{2\pi^{d/2}}{(2\pi)^{d/2}\Gamma(d/2)}\frac{p^{d-1}}{\sqrt{p^2+m_0^2}}\coth\left[\frac{\beta}{2}\sqrt{p^2+{m_0}^2}\right]. \tag{2.27}$$

Finally we differentiate both sides with respect to our rescaling parameter l

$$\frac{d\tilde{m}^2}{dl} = 2\tilde{m}^2 + \frac{\tilde{\lambda}}{4}\frac{2\pi^{d/2}}{(2\pi)^{d/2}\Gamma(d/2)}\frac{\coth\left(\frac{u\sqrt{1+\tilde{m}^2}}{2}\right)}{\sqrt{1+\tilde{m}^2}}, \tag{2.28}$$

where, as defined in Eq. 2.25, $u \equiv \beta\Lambda e^{-l}$ is the dimensionless measurement of the size in imaginary time, and we have taken $\tilde{\lambda_0}e^{-(d-3)l} = \tilde{\lambda}$, and $\tilde{m_0}^2 e^{2l} = \tilde{m}^2$.

2.3 The ϕ^4 coupling RG Equation

To calculate the RG equation for the coupling λ to one loop we must calculate the next term in the cumulant expansion $\langle S_{int}^2\rangle_H$. We first square Eq. 2.11

$$\langle S_{int}^2\rangle_H \approx \frac{\lambda_0^2\beta^2}{4!^2}\sum_{n1,\ldots,n6}\prod_{i=1}^{3}\prod_{i=5}^{7}\left[\int\frac{d^dk_i}{(2\pi)^d}\right]\langle(\tilde{\phi}_L\tilde{\phi}_L\tilde{\phi}_H\tilde{\phi}_H\tilde{\phi}_H\tilde{\phi}_H\tilde{\phi}_L\tilde{\phi}_L + ...)\rangle_H, \tag{2.29}$$

where the ... here denotes all possible permutations of the 8 field operators in the momentum variables as it did in Eq. 2.11, $\vec{k_4} = -(\vec{k_1}+\vec{k_2}+\vec{k_3})$, $n_4 = -(n_1+n_2+n_3)$, $\vec{k_8} = -(\vec{k_5}+\vec{k_6}+\vec{k_7})$,

and $n_8 = -(n_5 + n_6 + n_7)$. The three diagrams that correspond to this full expansion are depicted in Fig. 2.1 (b). Each one of these channels has a symmetry factor of 12 and each diagram contributes an equal amount to the renormalization of λ so we write

$$\langle S_{int}^2 \rangle_H \approx \frac{36\lambda_0^2\beta^2}{4!^2} \sum_{n1,\ldots,n6} \prod_{i=1}^{3} \prod_{i=5}^{7} \left[\int \frac{d^d k_i}{(2\pi)^d} \right] \tilde{\phi}_L \tilde{\phi}_L \langle \tilde{\phi}_H \tilde{\phi}_H \tilde{\phi}_H \tilde{\phi}_H \rangle_H \tilde{\phi}_L \tilde{\phi}_L, \tag{2.30}$$

which means that the correction to λ to one loop is given by

$$\delta\lambda = -\frac{36\lambda_0^2\beta}{4!} \sum_{n3,n5,n6} \int\int\int \frac{d^d k_3}{(2\pi)^d} \frac{d^d k_5}{(2\pi)^d} \frac{d^d k_6}{(2\pi)^d} \langle \tilde{\phi}_H \tilde{\phi}_H \tilde{\phi}_H \tilde{\phi}_H \rangle_H. \tag{2.31}$$

Computing the four point function and simplifying the expression yields

$$\delta\lambda = -\frac{3}{2\beta}\lambda_0^2 \sum_{n5,n6,n7} \prod_{i=3,5,6} \left[\int \frac{d^d k_i}{(2\pi)^d} \right] \frac{(2\pi)^{2d} \delta(\vec{k_3} + \vec{k_5}) \delta(\vec{k_4} + \vec{k_6}) \delta_{n_3+n_5} \delta_{n_4+n_6}}{(|\vec{k_3}|^2 + \omega_{n_3}^2 + m_0^2)(|\vec{k_6}|^2 + \omega_{n_6}^2 + m_0^2)}. \tag{2.32}$$

Integrating over the Dirac delta functions and the Kronecker deltas we have

$$\delta\lambda = -\frac{3}{2\beta}\lambda_0^2 \sum_n \int \frac{d^d k_3}{(2\pi)^d} \frac{1}{(|\vec{k_3}|^2 + \omega_{n_3}^2 + m_0^2)(|-\vec{k_1} - \vec{k_2} - \vec{k_3}|^2 + \omega_{n_4}^2 + m_0^2)}. \tag{2.33}$$

We Taylor expand this expression and extract the term that is independent of the external momentum and external Matsubara frequency–the reasoning behind this is twofold: our renormalized coupling constant should not depend on these arbitrary low energy parameters, and taking higher order terms in the Taylor expansion would generate terms that are increasingly irrelevant to our theory. With this prescription we have

$$\delta\lambda = -\frac{3}{2\beta}\lambda_0^2 \sum_n \int \frac{d^d p}{(2\pi)^d} \frac{1}{(|\vec{p}|^2 + \omega_n^2 + m_0^2)^2}. \tag{2.34}$$

Thus, integrating over the d-1 angular directions on the d-dimensional hypersphere, and using the fact that

$$\begin{aligned} \sum_{n=-\infty}^{\infty} \frac{1}{(|\vec{p}|^2 + (2\pi n/\beta)^2 + m_0^2)^2} = &\frac{\beta}{4(|\vec{p}|^2 + m_0^2)^{3/2}} \coth\left[\frac{\beta}{2} \sqrt{|\vec{p}|^2 + m_0^2} \right] \\ &+ \frac{\beta^2}{8(|\vec{p}|^2 + m_0^2)} \operatorname{csch}^2\left[\frac{\beta}{2} \sqrt{|\vec{p}|^2 + m_0^2} \right], \end{aligned} \tag{2.35}$$

we yield

$$\delta\lambda = -\frac{3}{8}\lambda_0^2 \frac{2\pi^{d/2}}{(2\pi)^{d/2}\Gamma(d/2)} \int_{b\Lambda}^{\Lambda} \frac{p^{d-1}dp}{(p^2+m_0^2)^{3/2}} \left(\coth\left[\frac{\beta}{2}\sqrt{p^2+m_0^2}\right] + \frac{\beta}{2}\sqrt{p^2+m_0^2}\mathrm{csch}^2\left[\frac{\beta}{2}\sqrt{p^2+m_0^2}\right]\right). \tag{2.36}$$

Following the procedure highlighted in section I we nondimensionalize our couplings, rescale, and differentiate with respect to our parameter l to yield the RG equation to one loop

$$\frac{d\tilde{\lambda}}{dl} = (3-d)\tilde{\lambda} - \frac{3}{8}\frac{2\pi^{d/2}}{(2\pi)^{d/2}\Gamma(d/2)}\frac{\tilde{\lambda}^2}{(1+\tilde{m}^2)^{3/2}} \left(\coth\left[\frac{u\sqrt{1+\tilde{m}^2}}{2}\right] + \frac{u\sqrt{1+\tilde{m}^2}}{2}\mathrm{csch}^2\left[\frac{u\sqrt{1+\tilde{m}^2}}{2}\right]\right) \tag{2.37}$$

2.4 The dimensionless temperature RG equation

The dimensionless measurement of imaginary time u has a trivial recursion formula

$$\frac{du}{dl} = -u, \tag{2.38}$$

which immediately follows from Eq. 2.25. We can define a dimensionless measurement of the temperature of the system, t, by the relationship

$$u = \frac{\tilde{\lambda}}{t}, \tag{2.39}$$

which means that

$$t = \frac{\tilde{\lambda}}{u} = \frac{\lambda\Lambda^{(d-3)}e^{(3-d)l}}{\beta\Lambda e^{-l}} = \lambda T \Lambda^{(d-4)} e^{(4-d)l}. \tag{2.40}$$

Using Eq. 2.38 and Eq. 2.39 gives

$$\frac{du}{dl} = -\frac{\tilde{\lambda}}{t} = \frac{d}{dl}\left(\frac{\tilde{\lambda}}{t}\right) = \frac{d\tilde{\lambda}}{dl}\frac{1}{t} - \frac{dt}{dl}\frac{\tilde{\lambda}}{t^2}, \tag{2.41}$$

which we solve for dt/dl. Doing some algebra and subbing in Eq. 2.37 yields

$$\frac{dt}{dl} = (4-d)t - \frac{3}{8}\frac{2\pi^{d/2}}{(2\pi)^{d/2}\Gamma(d/2)}\frac{\tilde{\lambda}t}{(1+\tilde{m}^2)^{3/2}} \left(\coth\left[\frac{\tilde{\lambda}\sqrt{1+\tilde{m}^2}}{2t}\right] + \frac{\tilde{\lambda}}{2t}\sqrt{1+\tilde{m}^2}\mathrm{csch}^2\left[\frac{\tilde{\lambda}\sqrt{1+\tilde{m}^2}}{2t}\right]\right). \tag{2.42}$$

2.5 RG Flows

Putting together the results of the last three sections, our RG equations are

$$\frac{d\tilde{m}^2}{dl} = 2\tilde{m}^2 + \frac{2}{3}\frac{\bar{\lambda}}{\sqrt{1+\tilde{m}^2}}\coth\left[\frac{\bar{\lambda}\sqrt{1+\tilde{m}^2}}{\bar{t}}\right], \tag{2.43}$$

$$\frac{d\bar{\lambda}}{dl} = (3-d)\bar{\lambda} - \frac{\bar{\lambda}^2}{(1+\tilde{m}^2)^{3/2}}\left(\coth\left[\frac{\bar{\lambda}\sqrt{1+\tilde{m}^2}}{\bar{t}}\right] + \frac{\bar{\lambda}\sqrt{1+\tilde{m}^2}}{\bar{t}}\mathrm{csch}^2\left[\frac{\bar{\lambda}\sqrt{1+\tilde{m}^2}}{\bar{t}}\right]\right), \tag{2.44}$$

$$\frac{d\bar{t}}{dl} = (4-d)\bar{t} - \frac{\bar{\lambda}\bar{t}}{(1+\tilde{m}^2)^{3/2}}\left(\coth\left[\frac{\bar{\lambda}\sqrt{1+\tilde{m}^2}}{\bar{t}}\right] + \frac{\bar{\lambda}\sqrt{1+\tilde{m}^2}}{\bar{t}}\mathrm{csch}^2\left[\frac{\bar{\lambda}\sqrt{1+\tilde{m}^2}}{\bar{t}}\right]\right). \tag{2.45}$$

where we have defined

$$\bar{\lambda} = \tilde{\lambda}\frac{3}{8}\frac{2\pi^{d/2}}{(2\pi)^{d/2}\Gamma(d/2)}, \tag{2.46}$$

and

$$\bar{t} = 2\frac{3}{8}\frac{2\pi^{d/2}}{(2\pi)^{d/2}\Gamma(d/2)}t. \tag{2.47}$$

To justify one's neglect of the higher loop terms in that arise in the cumulant expansion one typically takes $\epsilon = 3 - d << 1$ as the perturbative RG applies extremely well for all values of the parameters in the theory in this regime. In the following we characterize the quantum critical fan for $0 < \epsilon \leq 1$–for illustrative purposes we will take $\epsilon = 1$ in all plots of the RG flows and fans. Taking ϵ=1 implies that our perturbative expansion in λ is not very well controlled, but we carry on because the quantum critical fan is simpler to visualize at $\epsilon = 1$, and the results we yield will be quite close to those that one would obtain via other, more sophisticated, approaches to the problem such as using conformal field theory techniques. Taking $0 < \epsilon << 1$ yields the same qualitative physics as the case $\epsilon = 1$–the quantum critical fan will manifest itself in the same surface that we investigate for $\epsilon = 1$, but with a surface area which is merely scaled down by ϵ, and the theory will possess all of the same types of critical points at coupling strengths which are also scaled by ϵ. In other words, in both of these cases there exists a quantum critical point at zero temperature, above which a quantum critical fan is formed in a similar surface. For general $0 < \epsilon = 3 - d < 1$

the nontrivial fixed point of interest at $T = 0$ is given by

$$\bar{t}^* = 0, \quad \bar{\lambda}^* = \frac{3\epsilon}{3+\epsilon}\sqrt{1 - \frac{3\epsilon}{3+\epsilon}}, \quad \tilde{m^*}^2 = -\frac{\epsilon}{\epsilon+3}. \tag{2.48}$$

This is the quantum critical point. There is also the trivial fixed point at $\bar{t} = \bar{\lambda} = \tilde{m}^2 = 0$. We plot the flows (for $\epsilon = 1$) in several planes of interest in Fig.s 2.2, 2.3, 2.4, 2.5 below).

We linearize our RG equations to identify the leading order behavior near the quantum critical point and find that

$$\frac{d(\tilde{m}^2 - \tilde{m^*}^2)}{dl} \approx \left(2 - \frac{\epsilon}{3}\right)(\tilde{m}^2 - \tilde{m^*}^2), \tag{2.49}$$

$$\frac{d(\bar{\lambda} - \bar{\lambda^*})}{dl} \approx (\epsilon - 1)(\bar{\lambda} - \bar{\lambda^*}), \tag{2.50}$$

$$\frac{d\bar{t}}{dl} \approx \epsilon\bar{t}. \tag{2.51}$$

Here we see that $\bar{\lambda}$ is irrelevant at the quantum critical point for ϵ <1, and marginal at the quantum critical point when $\epsilon = 1$. To obtain the asymptotic behavior of the correlation length, and hence, the critical exponent, we integrate our recursion relations from $l = 0$ (where the dimensionless couplings are unrenormalized) up to the value l^* where the fastest growing coupling ($\tilde{m}^2, \bar{\lambda}$, or $\bar{t}$) reaches $O(1)$. Given this l^* we can "work backwards" and write our asymptotic correlation length in terms of the original UV cutoff ($\Lambda^{-1} \sim a$, where a is lattice spacing) as $\xi = ae^{l^*}$. Because the relevant couplings at the quantum critical point are $\tilde{m}^2$ and $\bar{t}$ (the relevant coupling dictate which recursion relation grows fastest) we can immediately identify the critical exponent ν_m via the linearized RG equations to be

$$\xi \approx \frac{a}{(\tilde{m}^2 - \tilde{m^*}^2)^{\nu_m}}, \qquad \nu_m = \frac{1}{2 - \epsilon/3}. \tag{2.52}$$

This correlation length expression is valid near criticality for $\bar{t} \to 0$ at $\bar{\lambda} = \bar{\lambda}^*$, and $(\tilde{m}^2 - \tilde{m^*}^2) < \delta$, where δ is an arbitrarily small, positive number.

This critical exponent is what one would typically get via other methods when studying the models in the Ising universality class. To gain some intuition on the physics in lower

dimensions we compare our results to those known for the 3D Ising model. The most rigorous methods of calculating ν_m have reported $\nu_m \approx 0.63$, whereas Eq. (2.52) predicts $\nu_m = 0.6$– and so for our simple and somewhat naive calculation at $\epsilon = 1$ we are still "close" to what is correct.

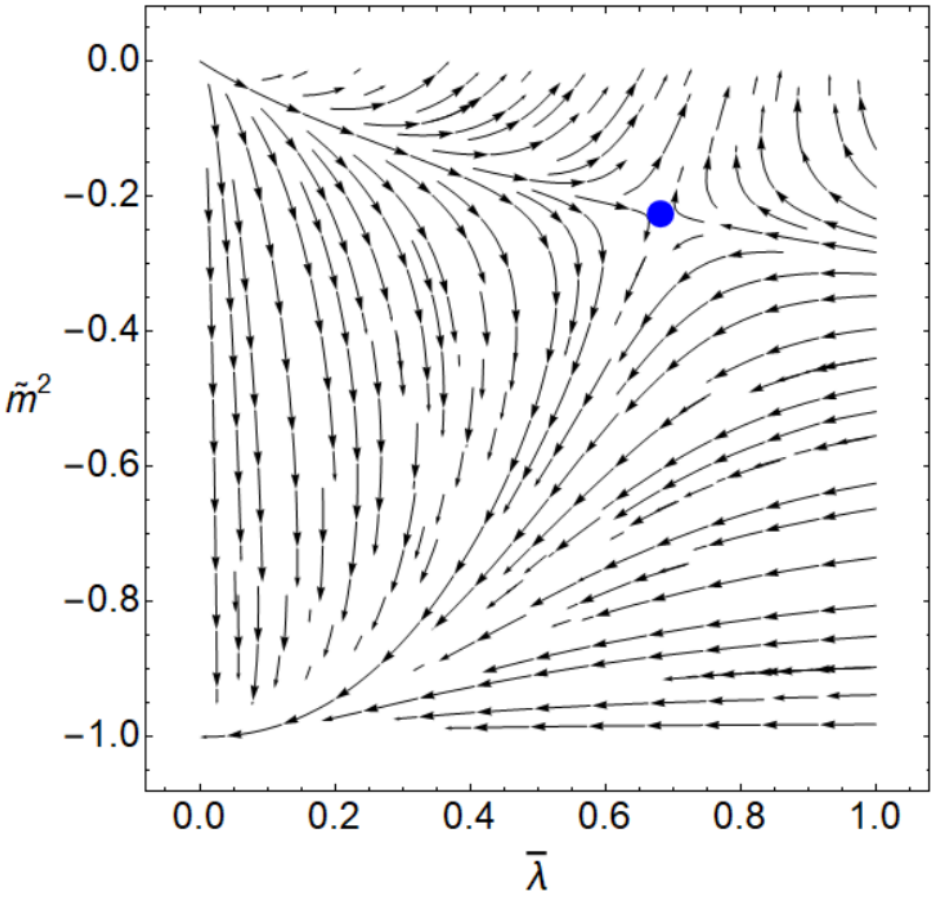

Figure 2.2: RG flows in the $\bar{\lambda}$-$\tilde{m}^2$ plane at $\bar{t} \to 0^+$. The blue dot indicates the quantum critical point at $\bar{\lambda}^*, \tilde{m^*}^2$.

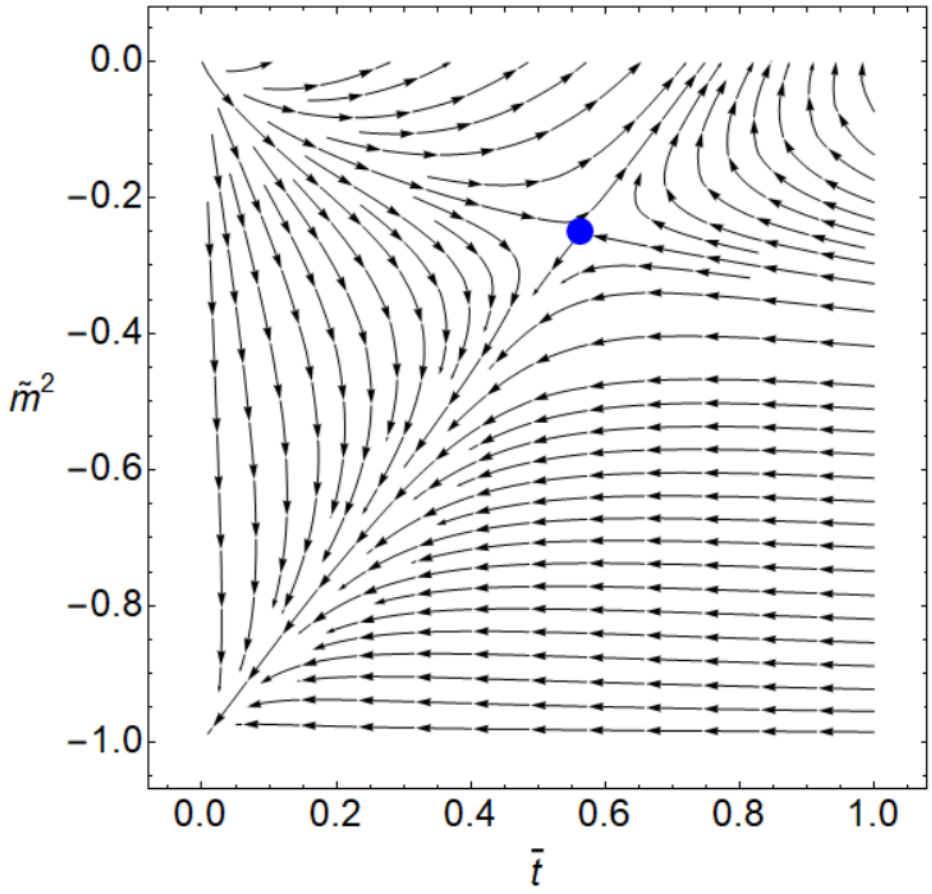

Figure 2.3: RG flows in the $\bar{t}$-$\tilde{m}^2$ plane at $\bar{\lambda} \to 0^+$. The blue dot indicates the fixed point $\bar{t}$, $\tilde{m}^2$=(9/16, -1/4).

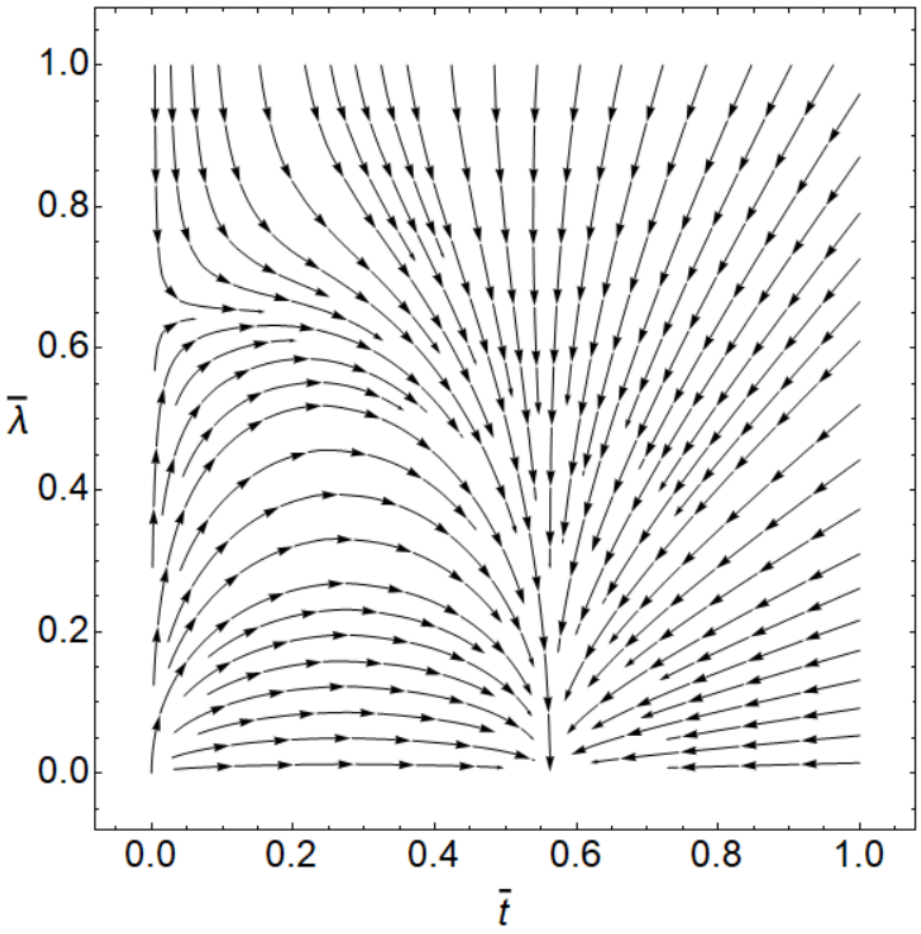

Figure 2.4: RG flows in the $\bar{t}$-$\bar{\lambda}$ plane with $\tilde{m}^2 = \tilde{m^*}^2$.

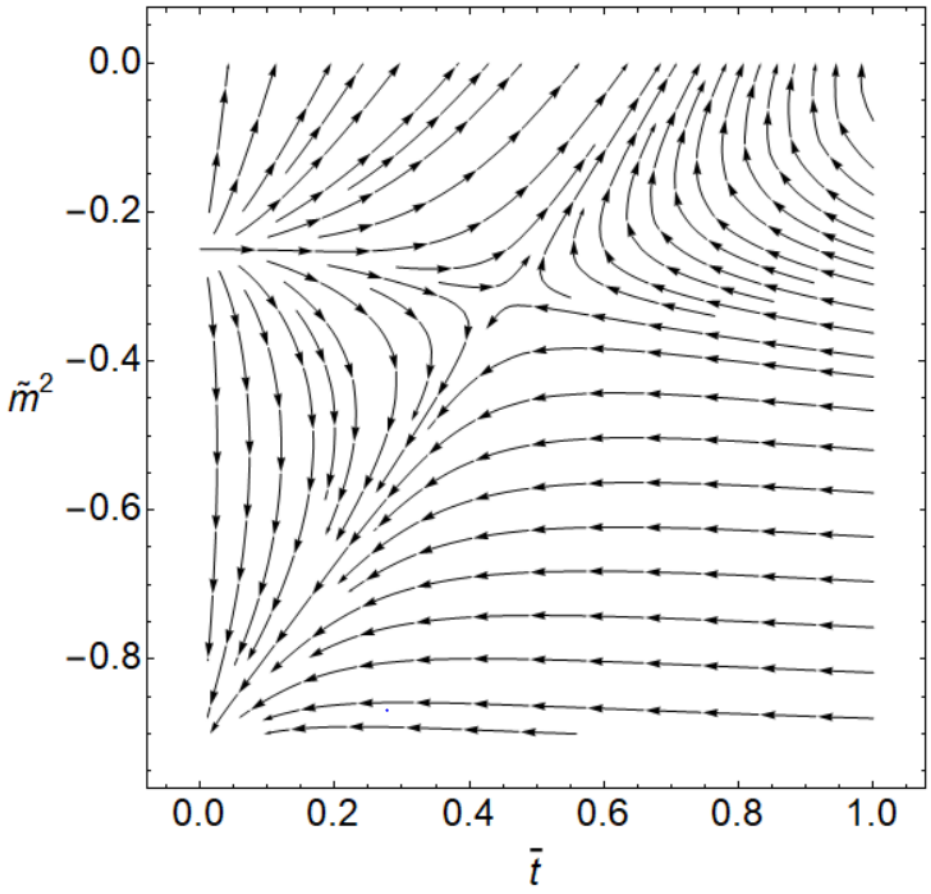

Figure 2.5: RG flows in the $\bar{t}$-$\tilde{m}^2$ plane at $\bar{\lambda} = \bar{\lambda}^*$.

2.6 The Quantum Critical Fan

One can characterize the RG parameter space into phases depending on the behavior of the correlation length [CHN89]. In the following we will characterize the quantum critical fan when $\epsilon = 1$. Taking $\epsilon = 1$ turns out to be convenient because $\bar{\lambda}$ is marginal at the quantum critical point, and hence does not initially flow upon lowering the momentum cutoff. Explicitly, for small values of the temperature at the critical value $\bar{\lambda}^*$, $\bar{\lambda}'$ is roughly zero for values of $\bar{t} < 0.2$. Hence, we investigate the $\bar{\lambda} = \bar{\lambda}^*$ plane for small values of $\bar{t}$.

Let us first begin by comparing the linearized RG equations of Eq.s (2.49), (2.50), (2.51) to understand which coupling sets the leading scale during the RG. The coupling space is divided in three regions: (I) Eq. (2.49) > Eq. (2.51), (II) Eq. (2.49) < Eq. (2.51), and (III) where $\tilde{m}^2 < \tilde{m^*}^2$. In region (III) the fields develop a vacuum expectation value (VEV) such that $\langle\phi\rangle \neq 0$–a phenomenon ubiquitous with spontaneous symmetry breaking–namely, the breaking of the discrete global $\mathbb{Z}_2$ symmetry of the original vacuum. In this case one must expand the fields, ϕ, about this VEV to understand the nature of the low lying energy excitations. Instead of working through a similar calculation to that done above for the case of a non-vanishing VEV we can simply label the region of coupling space "ordered" if the theory flows to the ordered fixed point at $\tilde{m}^2 = -1$, $\bar{t} = 0$ (where the VEV $\neq 0$). For case (II) the theory is in the quantum critical regime, where the most relevant parameter is the modified dimensionless temperature, $\bar{t}$. The borders of the fan can be identified as where the pertinent recursion relations roughly equal one another. Physically the argument follows that because the correlation length of the system near a quantum critical point diverges as $\xi^{-1} \approx (\tilde{m}^2 - \tilde{m^*}^2)^{\nu_m}$, there corresponds a vanishing energy scale $\Delta \sim \xi^{-z}$, where z is the dynamic critical exponent (z=1 for our particular theory of interest). Thus, the borders of our quantum critical fan are roughly given by the relationship

$$k_B T \sim \Delta \sim (\tilde{m}^2 - \tilde{m^*}^2)^{\nu_m}, \tag{2.53}$$

which identifies the quantum critical/quantum disordered crossover region. We plot the RG flows with the corresponding crossover curve in Fig. 2.6. The dashed lines in Fig. 2.6 are

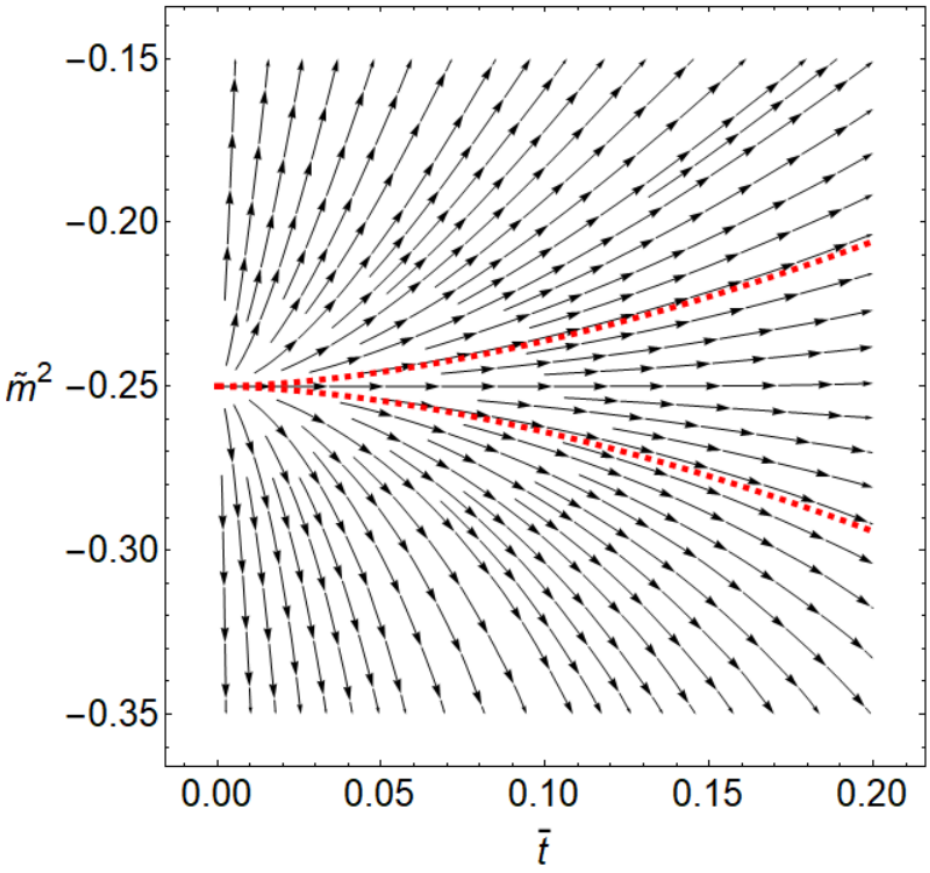

Figure 2.6: RG flows in the $\bar{t}$-$\tilde{m}^2$ plane at $\bar{\lambda} = \bar{\lambda}^*$ at low t. The three regions from top to bottom respectively are: I–the quantum disordered regime, II–the quantum critical regime, and III–the ordered regime.

given via Eq. (2.51) as $\bar{t}/(2\bar{\lambda}^*) = |(\tilde{m}^2 - \tilde{m^*}^2)|^{3/5}$.

Directly from Eq. (2.51) we have that the correlation length in the quantum critical region diverges as

$$\xi \sim a \left[\frac{1}{\bar{t}}\right]^{1/\epsilon}, \tag{2.54}$$

or, upon going to the only meaningful, nontrivial dimension by taking $\epsilon = 1$ and substituting in thermodynamic variables via our original definition of the dimensionless temperature,

$$\xi \sim \frac{1}{2\bar{\lambda}^* k_B T} = \frac{0.77}{k_B T}, \tag{2.55}$$

which is consistent with the idea that the correlation length universally diverges when ap-

proaching the quantum critical point in the quantum critical region as $\xi \sim 1/(k_B T)$. Restoring $\hbar$ and c we finally have that the correlation length behaves as

$$\xi \approx \frac{0.77\hbar c}{k_B T} \tag{2.56}$$

for low temperatures at $\lambda = \lambda^*$, $\tilde{m}^2 = \tilde{m^*}^2$.

CHAPTER 3

Density Wave States in the Presence of an External Magnetic Field

---

This chapter is adapted from the publication:

Powell, I. E., and Chakravarty, S. "Density Wave States in the Presence of an External Magnetic Field." Phys. Rev. B, **100**(7):075150, 27, August 2019

3.1 Preliminaries

Unlike Cooper pair condensation (particle-particle condensation) density wave states are comprised of particle-hole condensates. The particle-hole condensate wavefunction does not have to obey the same spin/orbital antisymmetry requirements that Cooper pair wavefunctions do because particles and holes are distinct objects. A particularly interesting density wave state is the $d_{x^2-y^2}$-density wave, also known as the staggered flux state. The staggered flux state breaks time-reversal symmetry and is visualized as a series of staggered currents on the bonds of the square lattice[Nay00a] (See Fig. 3.1). We briefly review particle-hole condensation in this angular momentum channel on the square lattice in the following.

On the mean field level the single particle Hamiltonian for electrons in an external magnetic field with singlet particle-hole pairing in the $d_{x^2-y^2}$ channel on the square lattice in

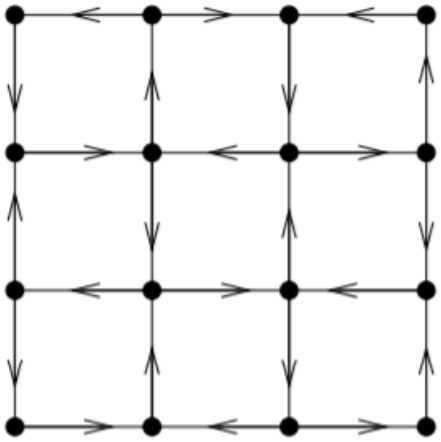

Figure 3.1: Real space lattice corresponding to the $d_{x^2-y^2}$ state. Arrowed lines indicate current.

position space is written as [JGC09, Hof76]

$$\begin{aligned} H = \sum_{n,m} & \left(-t_1 + i\frac{W_0}{4}(-1)^{n+m}\right) e^{i\phi_x}|m+1,n\rangle\langle m,n| \\ & + \left(-t_2 - i\frac{W_0}{4}(-1)^{n+m}\right) e^{i\phi_y}|m,n+1\rangle\langle m,n| \\ & -t_3 e^{i\phi_{xy}}|m+1,n+1\rangle\langle m,n| \\ & -t_4 e^{i\phi_{yx}}|m+1,n-1\rangle\langle m,n| + \text{H.C.} \end{aligned} \tag{3.1}$$

where each ϕ is the Peierls phase associated with each unique hopping element, W_0 is the d-density wave strength, we have subtracted off the chemical potential, and we have included only nearest neighbor (NN) and next-nearest neighbor (NNN) terms. For the remainder of the paper we take $t_1 = t_2 = t$, and omit spin indices.

When there is no external magnetic field present the staggered flux causes the unit cell's size to double–comprised of an $n+m =$ even, $n+m =$ odd. Ignoring NNN hopping we write the (gauge transformed) Hamiltonian in the absence of external magnetic field as

$$H = -\tilde{t}\sum_{n,m} e^{-2i\alpha_{nm}}|m+1,n\rangle\langle m,n| + |m,n+1\rangle\langle m,n| + \text{H.C.}, \tag{3.2}$$

where we have a new variable, $\tilde{t} = \sqrt{t^2 + (W_0/4)^2}$, and $\alpha_{nm} = \arctan(W_0/4t)(-1)^{n+m}$. In

this language the dispersion is written as

$$E = \pm 2\tilde{t}\sqrt{\cos^2(k_x) + \cos^2(k_y) + 2\cos(2\alpha)\cos(k_x)\cos(k_y)}, \tag{3.3}$$

where $\alpha = |\alpha_{nm}|$ and

$$\cos(2\alpha) = \frac{1 - (W_0/4t)^2}{1 + (W_0/4t)^2}. \tag{3.4}$$

We see that as the density wave strength is tuned on from 0 the dispersion evolves smoothly from the free electron case to the π-flux fermion case at $\alpha = \pi/4$. With this in mind we rewrite the Hamiltonian in the suggestive form

$$\begin{aligned} H = -\tilde{t}\sum_{n,m} e^{-2i\alpha_{nm}}|m+1,n\rangle\langle m,n| + \\ (\cos^2(2\alpha) + \sin^2(2\alpha))|m,n+1\rangle\langle m,n| + \text{H.C.}, \end{aligned} \tag{3.5}$$

which is equivalent to

$$H = \cos(2\alpha)H_0 + \sin(2\alpha)H_\pi, \tag{3.6}$$

where

$$H_0 = -\tilde{t}\sum_{n,m} |m+1,n\rangle\langle m,n| + \cos(2\alpha)|m,n+1\rangle\langle m,n| + \text{H.C.}, \tag{3.7}$$

and

$$\begin{aligned} H_\pi = -\tilde{t}\sum_{n,m} -i(-1)^{m+n}|m+1,n\rangle\langle m,n| + \\ \sin(2\alpha)|m,n+1\rangle\langle m,n| + \text{H.C.}. \end{aligned} \tag{3.8}$$

Here, H_0 is a a typical tight binding Hamiltonian, and H_π is a Hamiltonian for π-flux fermions.

3.2 Butterflies

3.2.1 Nearest Neighbors

Turning on an external magnetic field in the d-density wave problem amounts to the usual Peierls substitution [Pei33]. Taking the Landau gauge $\vec{A} = (-By, 0, 0)$, the m direction

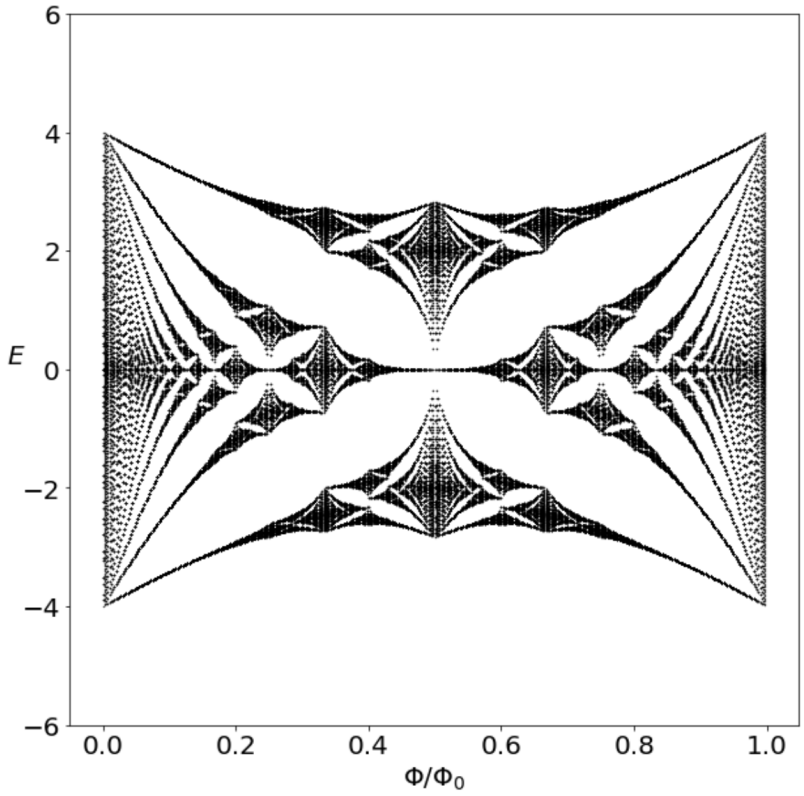

Figure 3.2: Plot of the butterfly for $\alpha = 0$.

hopping elements in the Hamiltonian (Eq. 3.5) are modified via $|m+1, n\rangle \rightarrow e^{-i2\pi n\Phi/\Phi_0}|m+1, n\rangle$, where $2\pi\Phi/\Phi_0$ is the dimensionless magnetic flux penetrating an elementary plaquette. We numerically diagonalize the Hamiltonian on a 20×20 lattice using periodic boundary conditions and plot the energy (in units of t) versus Φ/Φ_0 at the highest symmetry in Fig.s 3.2, 3.3 and 3.4.

When $\alpha = 0$ we recover the usual Hofstadter butterfly, and when $\alpha = \pi/4$ we recover the π-shifted butterfly governed by the form of Eq. 3.8. As α is tuned away from 0 linear Landau levels emerge from the edges of the spectrum at π flux, and relativistic levels emerge at 0 and 2π flux at charge neutrality yielding a spectrum similar to that of the honeycomb lattice[Ram85]. All emerging Landau levels are accompanied by gap openings with odd Chern number which will be discussed further in the following section. The relativistic

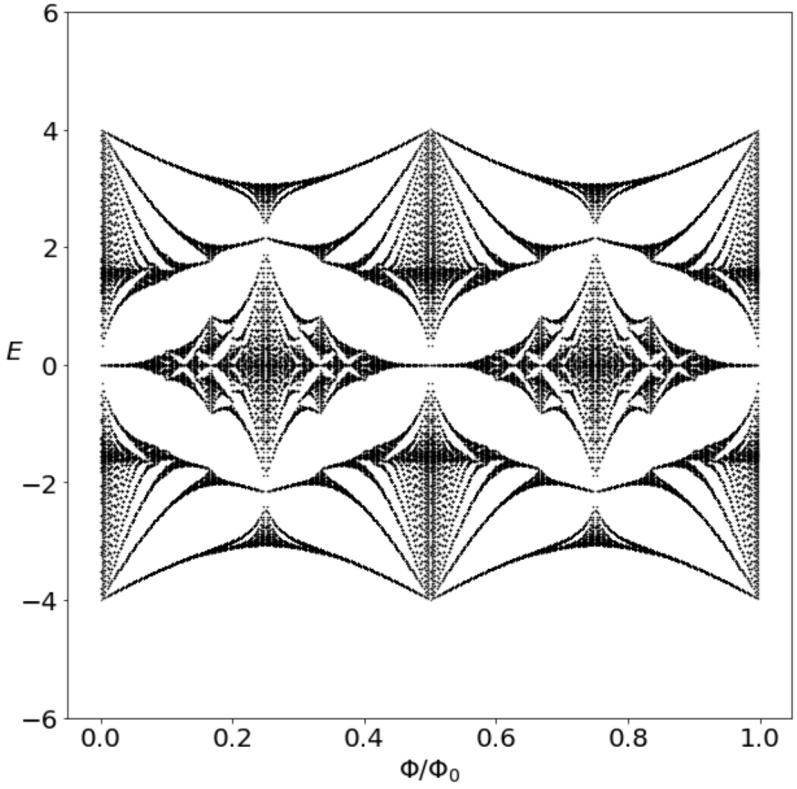

Figure 3.3: Plot of the butterfly for $\alpha = \pi/8$.

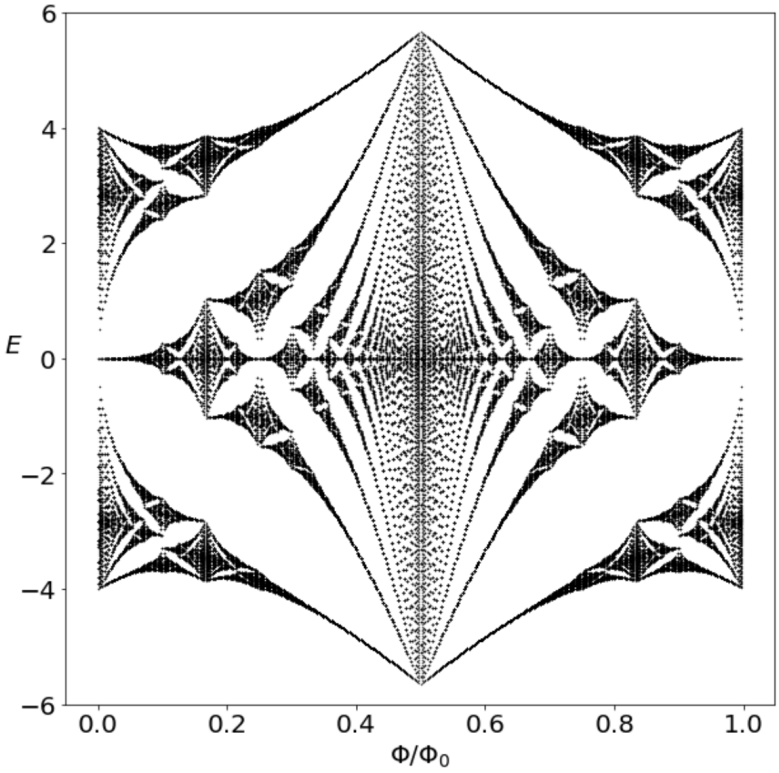

Figure 3.4: Plot of the butterfly for $\alpha = \pi/4$.

Landau level energy eigenvalues emerging from 0 flux are given by (see section 3.6)

$$\epsilon_n = \pm 2\sqrt{\frac{e_0 B|W_0|t}{c}n}. \tag{3.9}$$

As W_0 is tuned from 0 to $4t$ the Hall conductances, σ_{xy}, change for a given flux and Fermi energy. Due to the global nature of the transformation of the topological phase diagram (the Hofstadter butterfly) we categorize the topologically different types of Butterflies instead of investigating topological phase transitions local to a given flux and Fermi energy in the following section.

3.2.2 Topological Maps of the $d_{x^2-y^2}$-density wave Butterfly

To characterize the defining topological characteristics of each butterfly we start with the extremum of the transformation controlled by the density wave strength. First of all, consider the situation when $\alpha{=}\pi/4$. Directly from our Gauge transformed Hamiltonian we see that the total flux penetrating a plaquette is $\Phi \pm 4|\alpha| = \Phi \pm \pi$, where the plus or minus indicates that we are at an even/odd plaquette respectively. Thus the Hamiltonian can be written as

$$\begin{aligned} H = -\sqrt{2}t \sum_{n,m} & e^{-i(\Phi+\pi)n}|m+1,n\rangle\langle m,n| \\ & +|m,n+1\rangle\langle m,n| + \text{H.C.}, \end{aligned} \tag{3.10}$$

because the Hamiltonian in the absence of density wave condensation is symmetric about $\Phi = \pm\pi$.

This observation explicitly shows that the density wave parameter W_0 controls a smooth transformation between the typical butterfly and the π-shifted, or butterfly. The Hall conductances for the gaps can be written down immediately for these two extremum of the transformation via a Diophantine equation[TKN82], but because the particular Diophantine equation which governs the region $0 < \alpha < \pi/4$ is not immediately obvious we follow a different prescription.

To describe the global distribution of Chern numbers in the gaps of the butterflies we closely follow work done by Naumis[Nau16] on the "Cut and Projection" solution to the

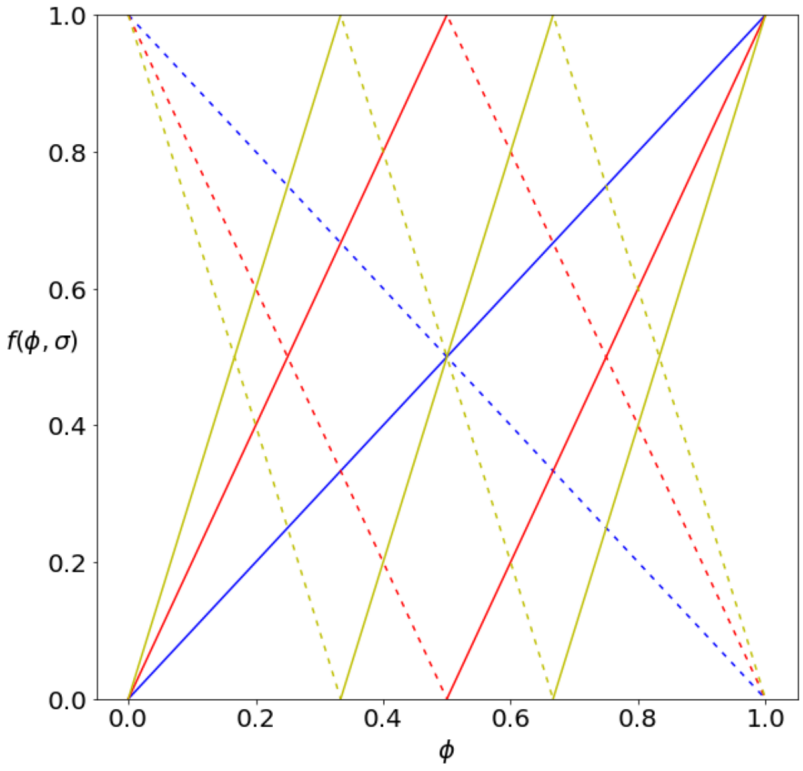

Figure 3.5: Skeleton of the butterfly for α=0. Solid (dashed) blue lines correspond to σ_{xy}=1 (-1), solid (dashed) red lines correspond to σ_{xy}=2 (-2), and solid (dashed) yellow lines correspond to σ_{xy}=3 (-3).

Diophantine equation

$$\sigma_r = q\left\{\phi r + \frac{1}{2}\right\} - \frac{q}{2}. \tag{3.11}$$

Here σ is the Hall conductance, r is the gap index, the curly braces indicate taking the fractional part of the quantity contained, and $\phi = \Phi/\Phi_0 = p/q$ where p/q is a fully reduced fraction. The filling factor for a gap's Chern number at a given flux is defined as

$$f(\phi, \sigma) = \{\phi\sigma_r\}. \tag{3.12}$$

Plotting $f(\phi, \sigma)$ against the flux yields the Wannier diagram[Wan78], or the "skeleton," of the butterfly. The form of $f(\phi, \sigma)$ dictates the distribution of Hall Conductances in the gaps of the butterflies. We find the skeletons for $\alpha = 0, \pi/4$ using this solution to the Diophantine equation (see Fig.s 3.5 and 3.6).

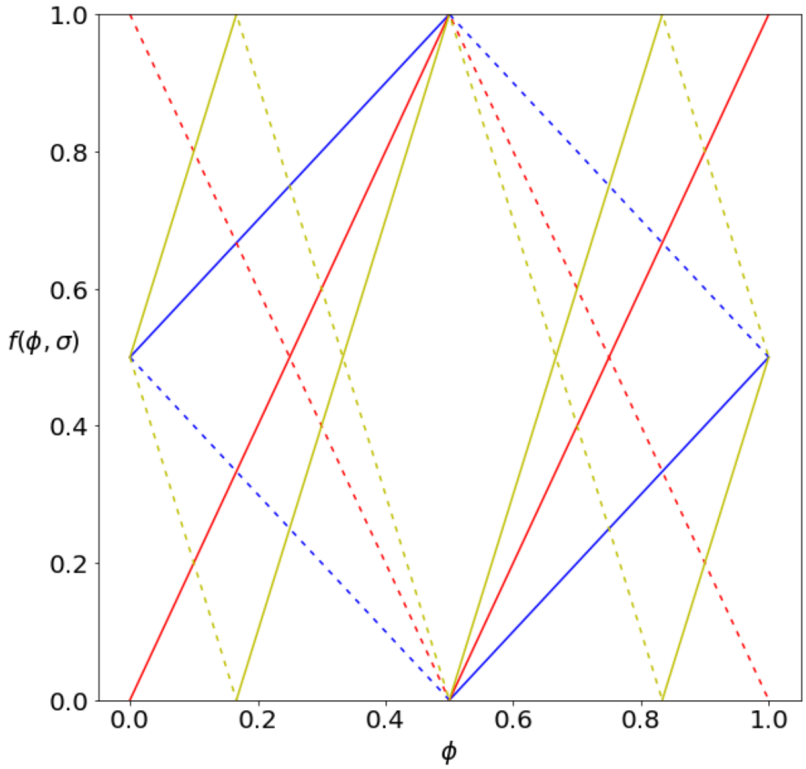

Figure 3.6: Skeleton of the butterfly for $\alpha = \pi/4$. Solid (dashed) blue lines correspond to σ_{xy}=1 (-1), solid (dashed) red lines correspond to σ_{xy}=2 (-2), and solid (dashed) yellow lines correspond to σ_{xy}=3 (-3).

To construct the Wannier diagram for values of $0 < \alpha < \pi/4$ we note the following: as soon as W_0 is nonzero all gaps that are not associated with the normal butterfly, but are associated with the π-flux butterfly, emerge (in section 3.6 we see that regardless of how small W_0 is all Landau levels indexed by n emerge). Furthermore, the Chern numbers associated with all gaps are topological invariants and thus will not change due to perturbations to the Hamiltonian. Taking these facts into account we draw the topological map for the region $0 < \alpha < \pi/4$ as the combination of the two extremum butterfly skeletons–see Fig. 3.7. Because our topological map is a combination of the normal butterfly skeleton and the π-shifted butterfly skeleton we see a doubling of lines associated with odd Hall Conductances, while the even Hall Conductances remain stationary.

At $\alpha = 0, \pi/4, \pi/2$ the odd numbered Hall band doubling dissapears, and one is left with

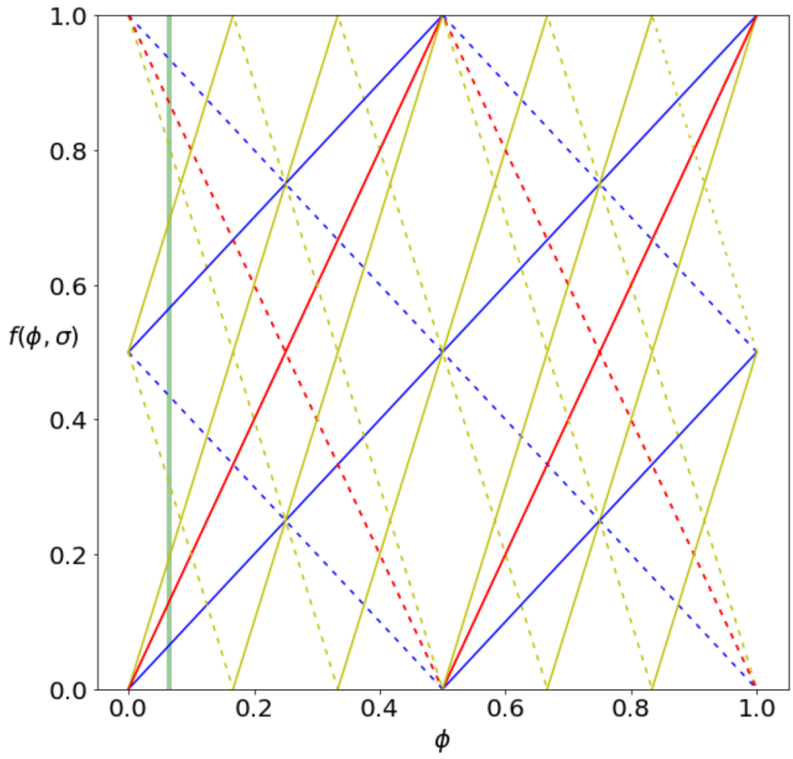

Figure 3.7: Skeletons of the butterflies for $0 < \alpha < \pi/4$. Solid (dashed) blue lines correspond to σ_{xy}=1 (-1), solid (dashed) red lines correspond to σ_{xy}=2 (-2), and solid (dashed) yellow lines correspond to σ_{xy}=3 (-3). The vertical green line acts as a guide–indicating that for the regime $0 < W_0 < 4t$, at a fixed flux, one would cross double the amount of odd Chern numbered gaps than those of the typical butterfly as one tunes the Fermi energy from the minimum value of the dispersion's energy to its maximum.

topological maps associated with Fig. 3.5. Notice, however, that α=$\pi/2$ is an unphysical region in which $W_0/t \to \infty$. Thus we see that there are three topologically distinct phase diagrams associated with the d-density wave problem in an external magnetic field, and that these maps change only at $W_0 = 0$, and $W_0 = 4t$.

Using the structure of our obtained diagrams as a guide we label the Hall conductances for all gaps associated with all butterflies (see Fig.s 3.8, 3.9, 3.10). Due to the odd Hall conductance line doubling for $0 < \alpha < \pi/4$ there exists a relativistic quantum Hall effect at low fields near charge neutrality (akin to that of Graphene[Y 05]) in the sense that the Hall

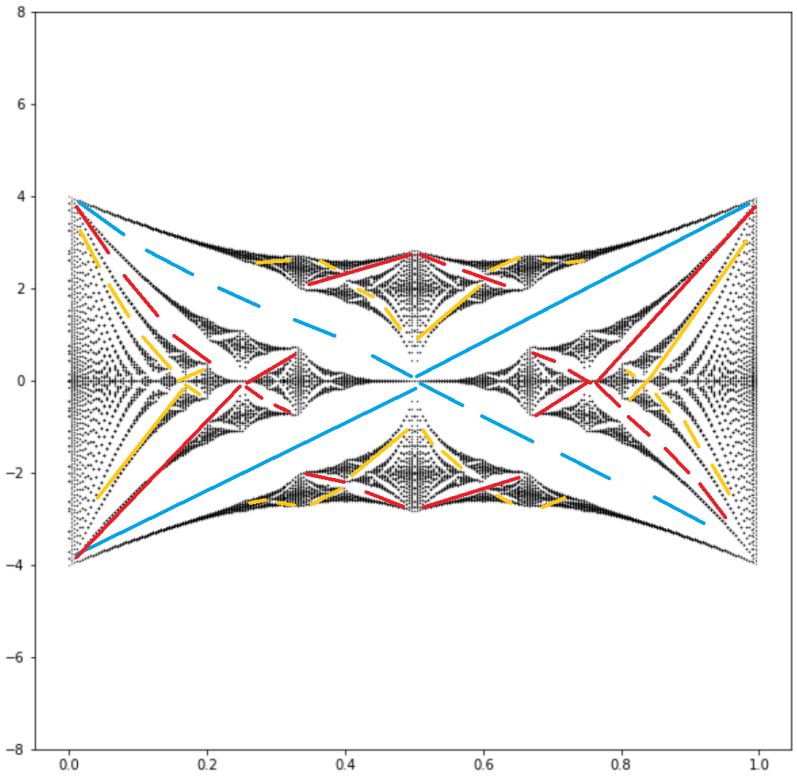

Figure 3.8: Butterfly with labeled characteristic Hall conductances for α=0 . Solid (broken) blue lines correspond to σ_{xy}=1 (-1), solid (broken) red lines correspond to σ_{xy}=2 (-2), and solid (broken) yellow lines correspond to σ_{xy}=3 (-3).

conductances are quantized via

$$\sigma_{xy} = \pm\frac{e^2}{h}2(2N+1), \tag{3.13}$$

where N is an integer and we have included a factor of 2 due to spin degeneracy. The typical integer Quantum Hall conductances persist at the edges of the spectrum near 0 flux and the odd Chern numbered gaps only dissapear completely when α=$\pi/4$ where the remaining gaps have

$$\sigma_{xy} = \pm\frac{e^2}{h}2(2N), \tag{3.14}$$

where, again, we have multiplied by a factor of 2 due to spin degeneracy.

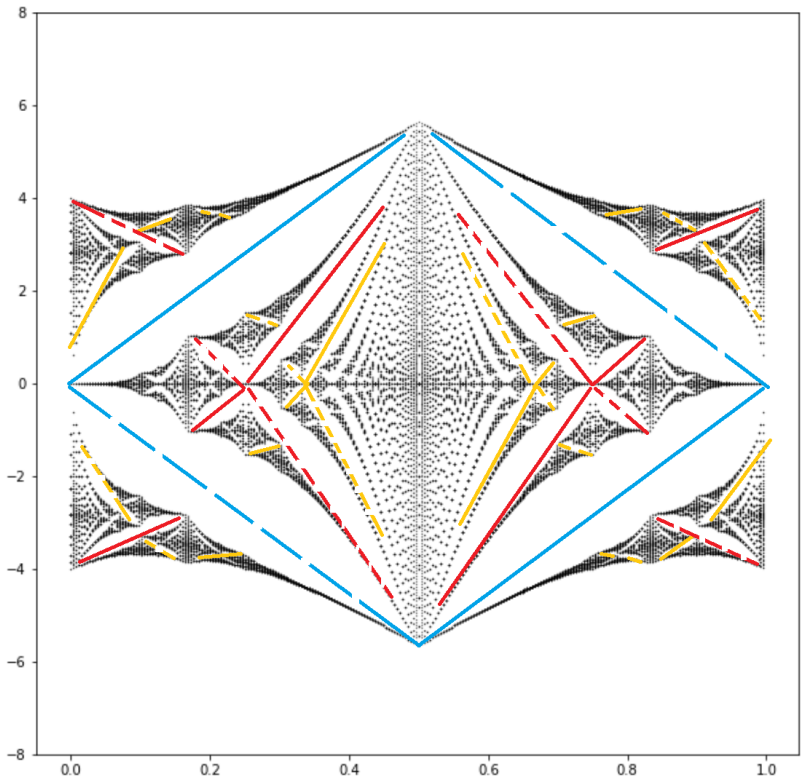

Figure 3.9: Butterfly with labeled characteristic Hall conductances for $\alpha=\pi/4$. Solid (broken) blue lines correspond to σ_{xy}=1 (-1), solid (broken) red lines correspond to σ_{xy}=2 (-2), and solid (broken) yellow lines correspond to σ_{xy}=3 (-3).

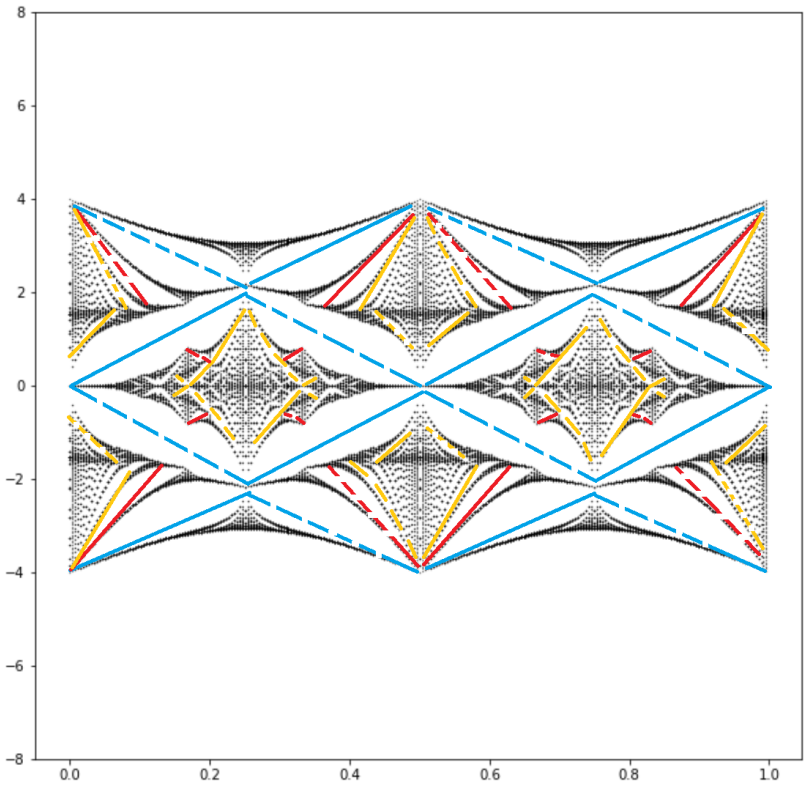

Figure 3.10: Butterfly with labeled characteristic Hall conductances for $\alpha=\pi/8$. Solid (broken) blue lines correspond to σ_{xy}=1 (-1), solid (broken) red lines correspond to σ_{xy}=2 (-2), and solid (broken) yellow lines correspond to σ_{xy}=3 (-3).

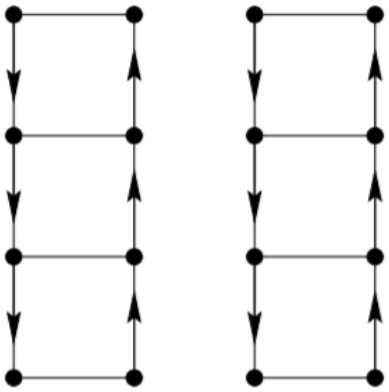

Figure 3.11: Real space lattice corresponding to the $p_x + ip_y$ density wave state. Arrowed lines indicate current whereas arrowless lines indicate bonds with no net current with energetically favored hopping.

3.3 $p + ip$ Density Wave Order

The singlet $\vec{Q}$=$(0, \pi)$ $p_x + ip_y$-density wave state also breaks translation and time-reversal symmetry, and is visualized as both a series of staggered currents pointing along the x direction, and bonds of zero net current that connect nearest neighbors along the y direction[Nay00a] (see Fig. 3.11). For this $\vec{Q}$=$(0, \pi)$ $p_x + ip_y$-density wave the Hamiltonian is

$$\begin{aligned} H = \sum_{n,m} \Big(-t - i\frac{W_0}{2}(-1)^n \Big) e^{i\phi_x} |m+1, n\rangle\langle m, n| \\ + \left(-t + \frac{W_0'}{2}(-1)^n \right) e^{i\phi_y} |m, n+1\rangle\langle m, n| + \text{H.C.} \end{aligned} \tag{3.15}$$

where the density wave order parameter is

$$\langle \psi^\dagger(\vec{k} + \vec{Q})\psi(\vec{k})\rangle = \pm(W_0 \sin(k_x) + iW_0' \sin(k_y)). \tag{3.16}$$

In the following we take $W_0 = W_0'$, and define $\alpha = \arctan(\frac{W_0}{2t})$. We plot the butterflies at two characteristic points for a 20×20 lattice in Figs. 3.12, and 3.13. We see that chiral p-density wave condensation breaks the butterfly's reflection symmetry about π flux, opens bubbles of $\sigma_{xy} = 0$, and causes major band gaps to collapse (a phenomenon well

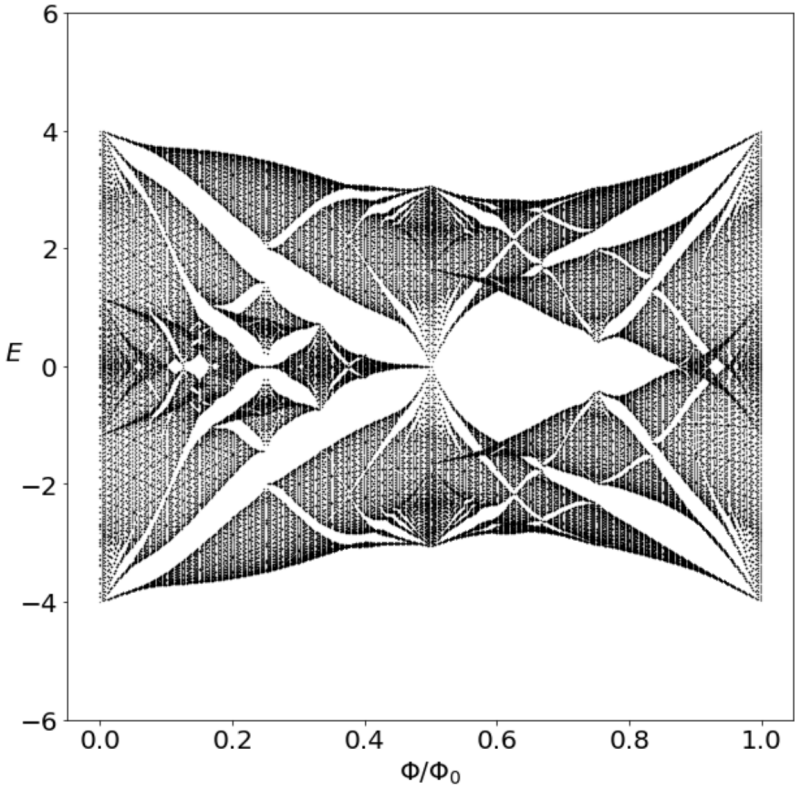

Figure 3.12: Plot of the butterfly for $\alpha = \pi/8$.

known to occur in lattices with anisotropic hoppings[HHK90])–in fact, at α=$\pi/4$, when the system is completely dimerized along the y direction and the lattice is composed of disjointed $2\times L$ (L being the side length of the lattice along the x direction in units of the lattice constant) cylindrical strips of alternating density wave induced fluxes, we find that the butterfly is completely destroyed and all gaps have collapsed except for a major gap near charge neutrality emanating from π flux. For the $p - ip$-density wave case the spectrum is obtained via a reflection of the $p + ip$ spectrum about π flux–implying that the $\sigma_{xy} = 0$ gap would be detectable at modest magnetic field strengths. For either type of chiral p-wave condensation at $W_0 = 2t$ the electrons would not obey any type of Landau quantization of their cyclotron orbits. Furthermore, because Chern numbers follow a "zero sum" rule, this major gap at $\alpha = \pi/4$ must have $\sigma_{xy} = 0$–thus, using the arguments highlighted in the previous section, the topological map of Hall conductances associated with this density wave state for $0 < W_0 < 2t$ is given by the typical square lattice skeleton (Fig. 3.5) and a

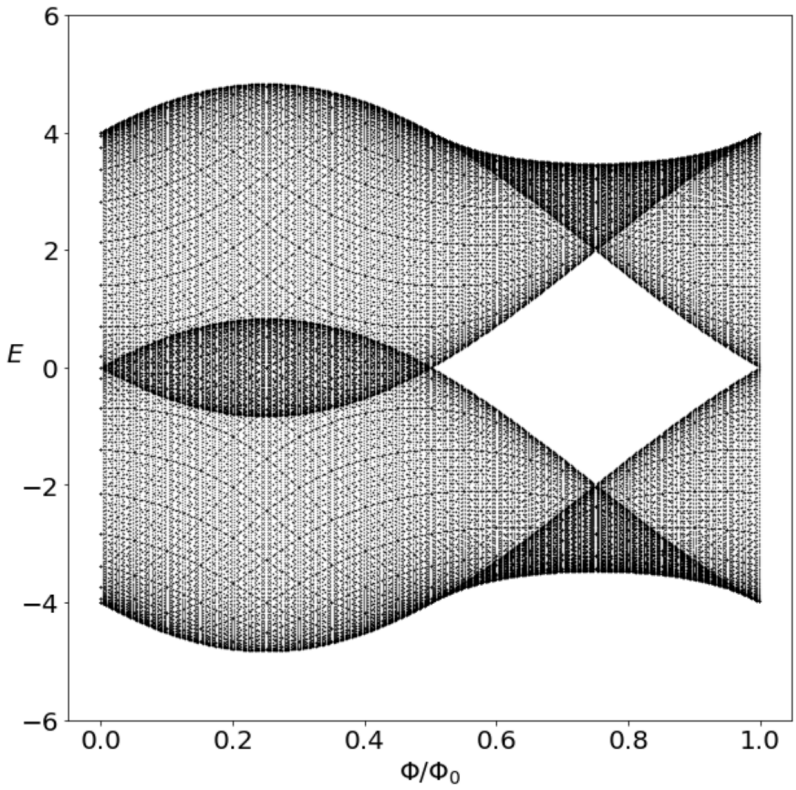

Figure 3.13: Plot of the butterfly for $\alpha = \pi/4$.

$f(\phi, \sigma) = 0$ line.

3.4 Multifractal Analysis

Multifractality is a defining characteristic of wave function fluctuations at criticality[EM08]. In the following we investigate the nature of the quantum phase transitions that occur as we increase the density wave strength utilizing a basic multifractal analysis of the generalized inverse participation ratio. Via this procedure we find that, at a fixed value of magnetic flux, the zero-energy eigenfunctions undergo metal-metal transitions separated by energy level crossings and single particle wave function multifractality.

The generalized inverse participation ratio (IPR) scales with the system size

$$P_q = \sum_{m,n} |\psi(r_{m,n})|^{2q} \sim L^{-\tau(q)} \tag{3.17}$$

at a fixed energy, where the summation is taken over the real space lattice defined by $r_{m,n}$. The exponents $\tau(q)$, indexed by a continuous variable q, are given by $\tau(q) = D_q(q-1)$, where $D_q = d$ for delocalized metallic states and D_q=0 for exponentially localized insulating states. Exponents $\tau(q)$ that depend on q in a nonlinear fashion indicate wave function multifractalilty. In our analyses we focus on the behavior of the system near charge neutrality–thus, to obtain the wave functions pertinent to Eq. 3.17, we diagonalize the magnetic Hamiltonian in real space (as we did when plotting the butterflies) and find the corresponding zero energy eigenvectors of the system for a fixed pair of Φ, and W_0.

We choose values of Φ/Φ_0 such that there exists a zero energy eigenvalue for all W_0. Numerically there is a difficulty in calculating the IPR of a single degenerate energy eigenvector. To remedy this we add a small amount of flux Δ=1×10^{-15} to Φ/Φ_0 which does not alter the spectrum, or eigenvectors in any appreciable manner but does separate (on the order of Δ) the degenerate zero energy eigenvalues from one another enough for us to calculate the IPR of a single zero energy eigenvector as a function of W_0 without mixing in the IPR of the other degenerate zero energy eigenvectors.

As W_0 is tuned a level crossing occurs in the spectrum. At this (highly degenerate) crossing point the Chern numbers of the bands participating are no longer well defined, but still follow the requirement that the sum of all Cherns in the spectrum is zero. For a 28×28 lattice we plot both the spectrum and the IPR($q = 2$) at $\Phi/\Phi_0 = 1/4 + \Delta$ (see Fig.s 3.14 and 3.15). All listed values of W_0 are in units of t. At this particular flux there is an energy level crossing which occurs at $W_0^* = 4\tan(\frac{\pi}{8})$ which is accompanied by a singular behavior of the IPR($q = 2$)–indicating a rapid change in the behavior of the single particle wave function fluctuations at the point where the energy levels touch. We find that the multifractal exponents reveal that the zero energy wave functions demonstrate multifractality at W_0^*–see Fig. 3.16, and Fig. 3.17. The behavior of the multifractal exponents at this critical point indicate a weakly multifractal behavior (sometimes dubbed "quasimetallic") with $\tau(q)$'s leading nonlinear dependence (found using a least squares fitting method) $\approx -0.115q(q-1)$ in the region $0 < q < 3$. Furthermore, we find that on either

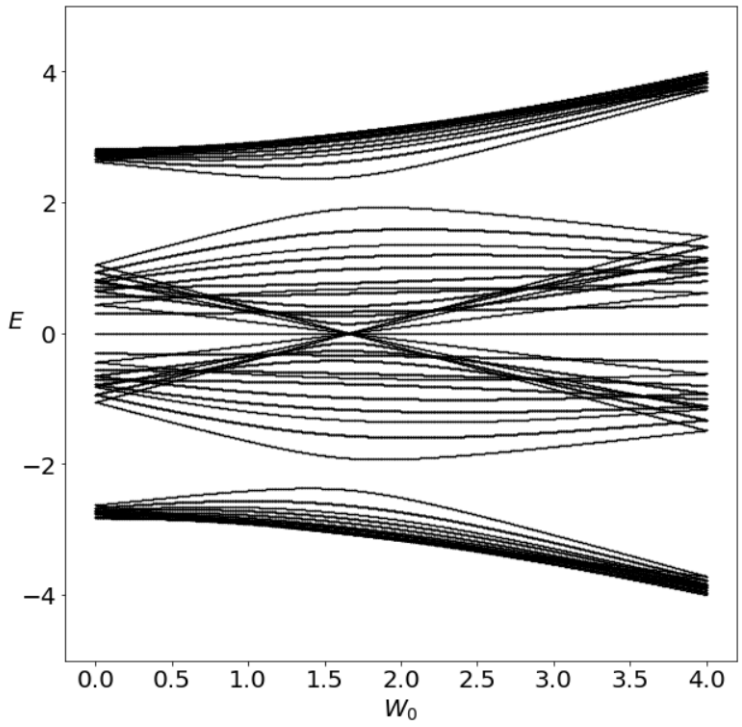

Figure 3.14: Energy versus d-density wave strength calculated at $\Phi/\Phi_0 = 1/4$ for a 28×28 lattice.

side of the critical point $\tau(q) \approx 2(q-1)$ which is a signature of delocalized metallic states in two spatial dimensions. Due to both the level crossing and the real space multifractality of the wavefunctions near the central peak shown in Fig. 3.15, we find that the d-density wave strength controls a metal-metal transition at $\Phi/\Phi_0 = 1/4 + \Delta$ at charge neutrality.

Physically this critical point, which is generally given by $W_0^* = 4t\text{Tan}\left(\pi\frac{\Phi}{2\Phi_0}\right)$ for arbitrary Φ/Φ_0, marks the point at which the local effective magnetic fields penetrating neighboring plaquettes flip from aligned to anti-aligned (see Fig. 3.18). This can be seen directly by calculating the total effective dimensionless flux $2\pi\Phi_T/\Phi_0$ per plaquette utilizing the phase factor in Eq. 3.2

$$2\pi\Phi_T/\Phi_0 = 2\pi\Phi/\Phi_0 \pm 4\alpha. \tag{3.18}$$

For $W_0 < W_0^*$ the flux per plaquette is alternaing but always positive. At $W_0 = W_0^*$ the flux alternates between $4\pi\Phi/\Phi_0$ and 0. For $W_0 > W_0^*$ the total effective flux per plaquette is alternaing in magnitude and sign (see Fig. 3.18).

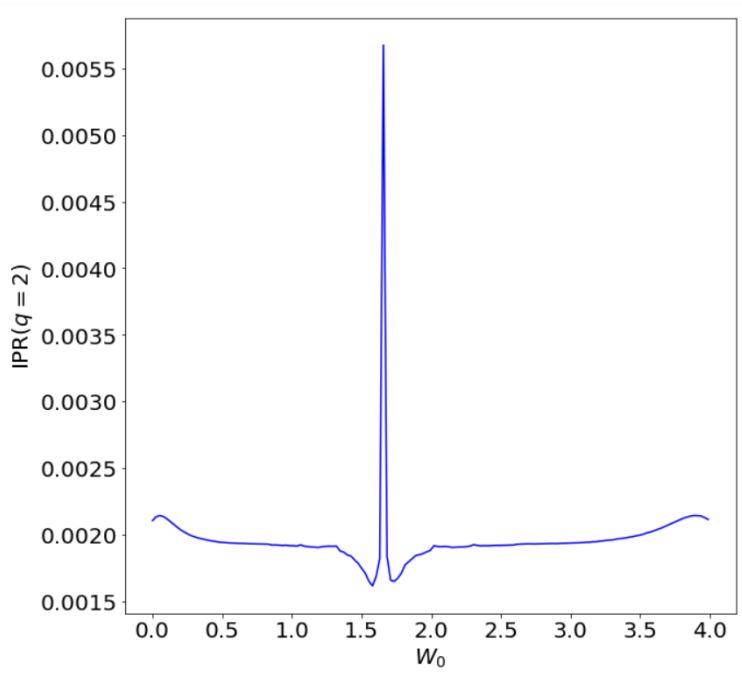

Figure 3.15: Numerically calculated IPR (q=2) as a function of W_0 of one of the zero energy wave functions for a 28×28 lattice at $\Phi/\Phi_0 = 1/4 + \Delta$.

For the case of $p + ip$-density wave condensation wavefunctions tend to behave in a localized fashion at W_0=2 for all $\Phi > 0$ due to the dimerization that occurs in the lattice along the y direction. We calculate the wavefunctions' multifractal exponents at charge neutrality as we did in the d-density wave case and plot the spectrum and IPR with Φ fixed in Fig.s 3.19 and 3.20. The wavefunctions in this case display strong multifractality at W_0=2 (see Fig. 3.21) where the electrons are strongly localized to a strip of the lattice and there is another level crossing similar to that observed in the d-density wave case. For W_0=2 we find the nonlinear dependance of $\tau(q) \approx 0.503q^2 + 2.60\sqrt{q}$ for $0 < q < 1$ using the fitting method mentioned above.

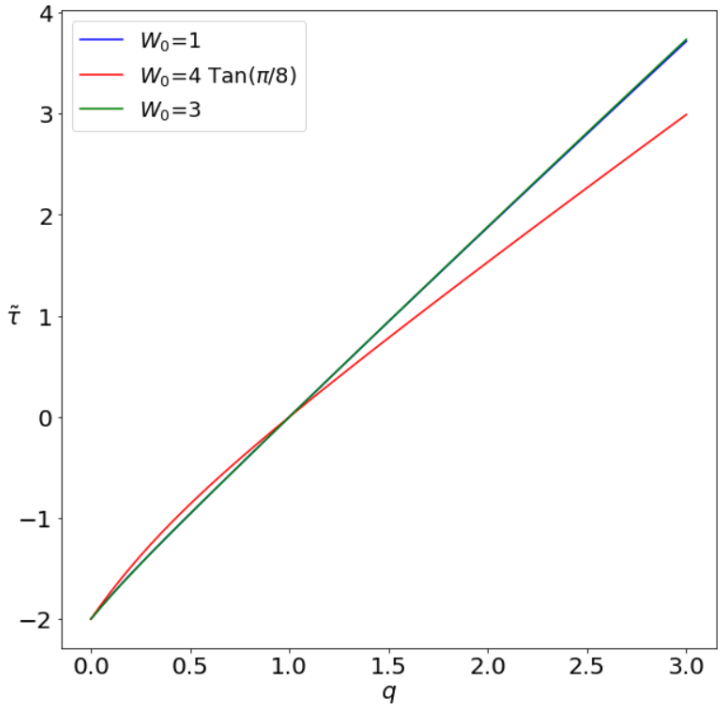

Figure 3.16: Values of -ln(P_q)/ln(L) = $\tilde{\tau}(q)$ calculated for a 28×28 lattice at $\Phi/\Phi_0 = 1/4+\Delta$ for three characteristic values of W_0.

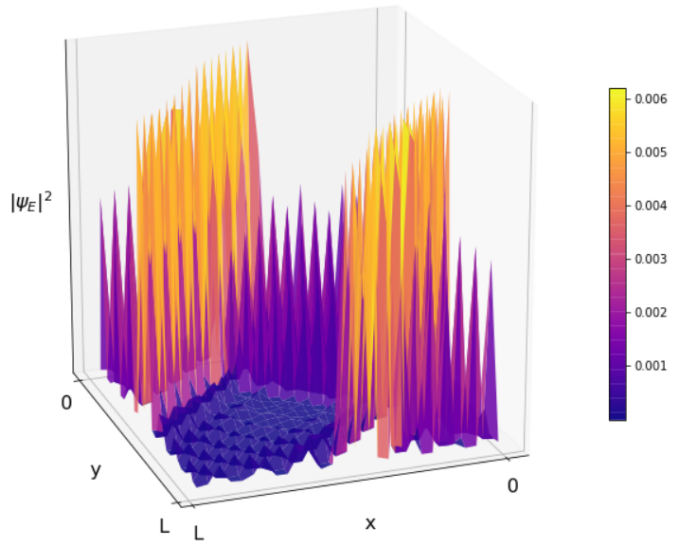

Figure 3.17: The probability density of a zero energy critical wavefunction calculated on a 28×28 lattice at $\Phi/\Phi_0 = 1/4 + \Delta$.

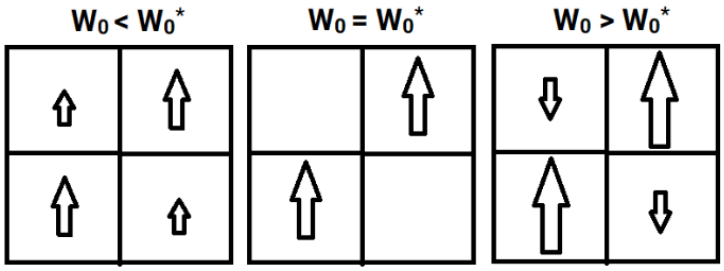

Figure 3.18: Pictorial representation of the local magnetic field (perpendicular to the lattice) per plaquette for different values of W_0 for the d-density wave case. The size of the arrow indicates the strength of the field.

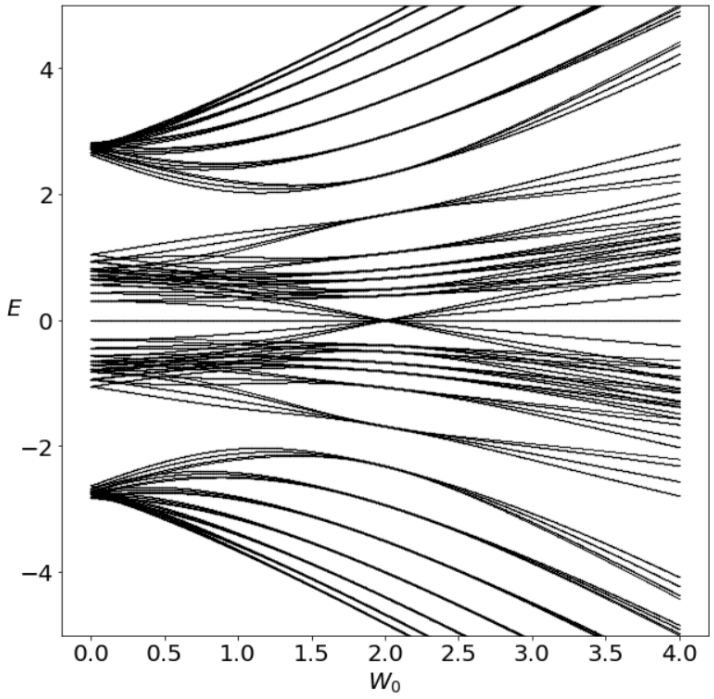

Figure 3.19: Energy versus $p + ip$-density wave strength calculated at $\Phi/\Phi_0 = 1/4$ for a 28×28 lattice.

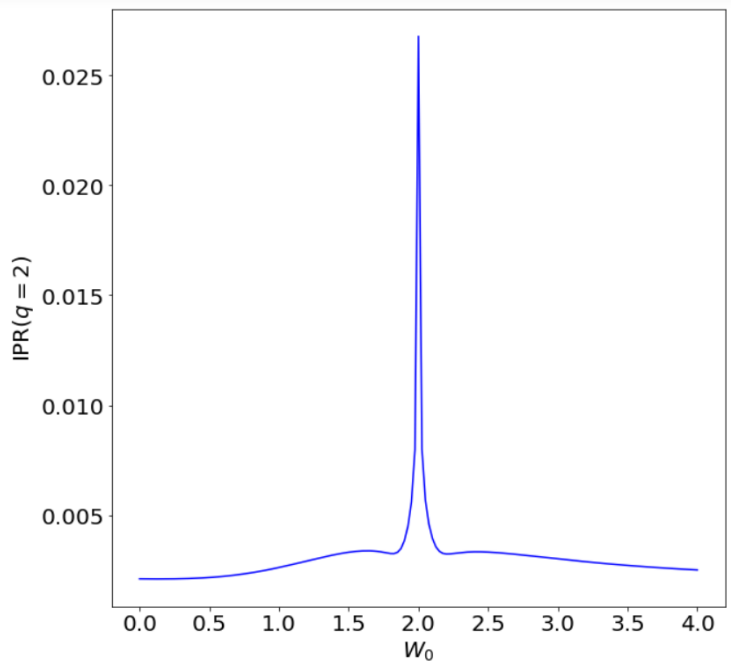

Figure 3.20: Numerically calculated IPR (q=2) as a function of W_0 of one of the zero energy wave functions for a 28 × 28 lattice at $\Phi/\Phi_0 = 1/4 + \Delta$.

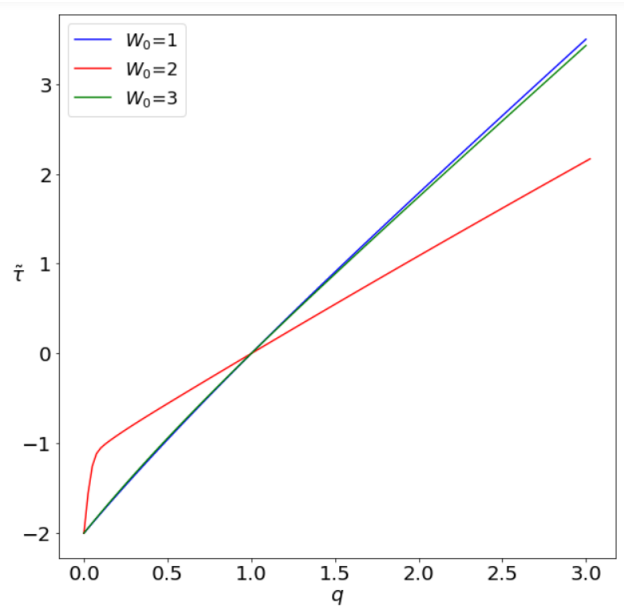

Figure 3.21: Values of -ln(P_q)/ln(L) = $\tilde{\tau}(q)$ calculated for a 28×28 lattice at $\Phi/\Phi_0 = 1/4+\Delta$ for three characteristic values of W_0.

3.5 Discussion

In this work we have studied and characterized the topologically different forms of the Hofstadter butterflies generated in the presence of density wave condensations in the $d_{x^2-y^2}$, and $p_x \pm ip_y$ angular momentum channels and investigated the quantum phase transitions that occur at charge neutrality as density wave strength increases. Directly from the skeleton diagrams obtained for the $d_{x^2-y^2}$-density wave problem we see a doubling in the odd-Hall conductance lines which implies that the density wave strength controls a relativistic quantum Hall effect with $\sigma_{xy}=\pm\frac{e^2}{h}2(2N+1)$. Furthermore, we find that the $p+ip$-density wave both causes band gap collapses in the butterfly, and causes the opening of 0 Hall conductivity bubbles. The effects of density wave states in the presence of an external magnetic field can be detected both at modest magnetic field strengths in 2D square crystal lattices (via a measurement of an unusual quantum Hall effect for the d-wave, or via a measurement of the system which shows both a lack of Landau levels and the opening of $\sigma_{xy}=0$ gaps near charge neutrality), and in optical lattice systems with the appropriate staggered fluxes present.

Our results have shown that different types of metal-metal transitions, controlled by density wave strength and separated in phase space by single particle wavefunctions exhibiting multifractality, would be detectable in systems emulating density wave states at non-zero flux at half filling. These quantum phase transitions occur generically for both density wave condensations due to the nonanalyticity introduced when the energy levels cross in the spectrum at strip dimerization for $p+ip$-density waves, or at the critical value of the staggered flux at $W_0^* = 4t\,\tan\left(\frac{\pi\Phi}{2\Phi_0}\right)$ for d-density waves. We note that in the presence of moderate disorder the energy levels would be broadened but the physics outlined in our work would be effectively the same–the effects of strong disorder on the other hand should be considered in future work. Furthermore, future work might also investigate how mutual Coulomb interactions would affect the multifractal wavefunctions and quantum phase transitions that occur as a function of density wave strength.

3.6 Appendix: Landau Levels

To see how the relativistic Landau Levels emerge in the spectrum we follow the standard analysis[McC56] and expand the tight binding Hamiltonian in the even-odd basis

$$H_0(\vec{k}) = -2\tilde{t}\begin{bmatrix} 0 & e^{-2i\alpha}\cos(k_x)+\cos(k_y) \\ e^{2i\alpha}\cos(k_x)+\cos(k_y) & 0 \end{bmatrix} \tag{3.19}$$

about one of the charge neutrality points $\vec{k}$=$(\pi/2, \pi/2)$

$$H_0(\vec{k}) \approx 2\tilde{t}\begin{bmatrix} 0 & e^{-2i\alpha}k_x+k_y \\ e^{2i\alpha}k_x+k_y & 0 \end{bmatrix}. \tag{3.20}$$

When introducing a magnetic field one makes the substitution

$$k_x \to k_x + \frac{eBy}{c} = \tilde{k}_x, \tag{3.21}$$

where e is the electron's charge and c is the speed of light. Because $\hat{k}_y$ and $\hat{y}$ do not commute with one another we place hats on all crystal momentum and position variables in the Hamiltonian with the understanding that we will work in the real space ($\hat{k}_y = -i\partial_y$) representation of these operators henceforth. Rearranging the Schrödinger equation

$$2\tilde{t}\begin{bmatrix} 0 & e^{-2i\alpha}\hat{\tilde{k}}_x+\hat{k}_y \\ e^{2i\alpha}\hat{\tilde{k}}_x+\hat{k}_y & 0 \end{bmatrix}\begin{bmatrix}\psi_n \\ \phi_n\end{bmatrix} = \epsilon_n\begin{bmatrix}\psi_n \\ \phi_n\end{bmatrix} \tag{3.22}$$

yields two decoupled wave equations

$$\epsilon_n^2\psi_n = 4\tilde{t}^2(e^{-2i\alpha}\hat{\tilde{k}}_x+\hat{k_y})(e^{2i\alpha}\hat{\tilde{k}}_x+\hat{k_y})\psi_n, \tag{3.23}$$

$$\epsilon_n^2\phi_n = 4\tilde{t}^2(e^{2i\alpha}\hat{\tilde{k}}_x+\hat{k_y})(e^{-2i\alpha}\hat{\tilde{k}}_x+\hat{k_y})\phi_n. \tag{3.24}$$

For the time being we solve Eq. 3.23. Foiling out this wave equation we yield

$$\begin{aligned}\frac{\epsilon_n^2}{4\tilde{t}^2}\psi_n(y,k_x) = \Big(\big(\hat{k_x}+\frac{eB\hat{y}}{c}\big)^2+\hat{k_y}^2+ \\ \cos(2\alpha)\{\hat{k_x}+\frac{eB\hat{y}}{c},\hat{k_y}\}-i\sin(2\alpha)\frac{eB}{c}[\hat{y},k_y]\Big)\psi_n(y,k_x),\end{aligned} \tag{3.25}$$

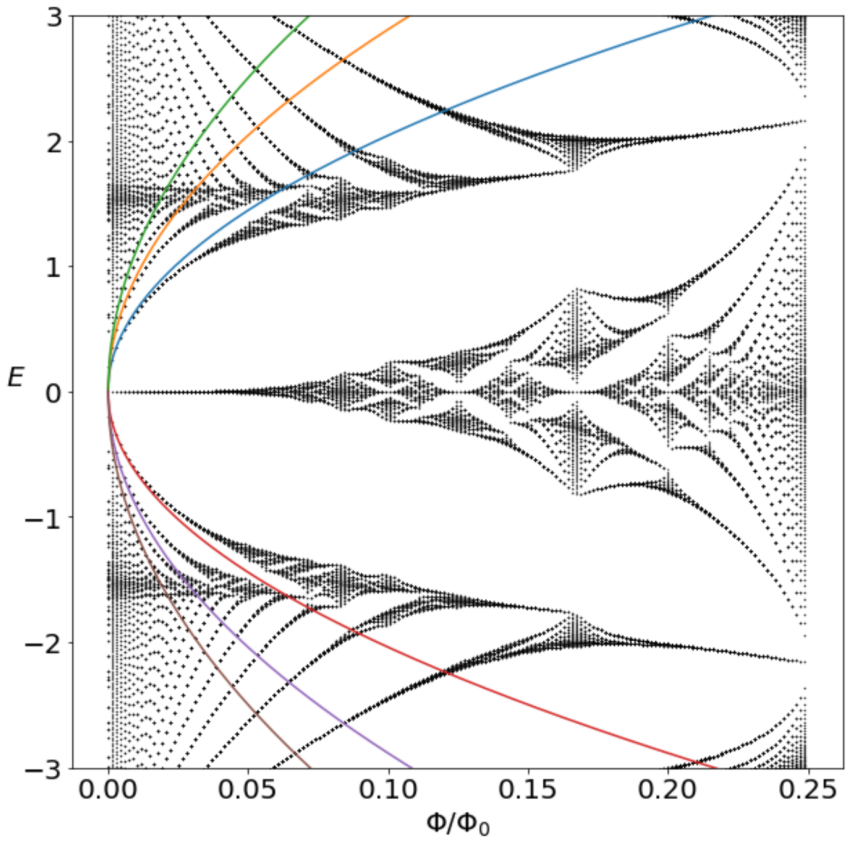

Figure 3.22: Plot of the butterfly and the associated first few nonzero Landau levels for $\alpha{=}\pi/8$.

where we have used the fact that $[\hat{k_x}, \hat{k_y}] = 0$.

We define

$$y_0 = k_x \frac{c}{e_0 B}, \quad \omega = \frac{e_0 B}{mc}, \tag{3.26}$$

where e_0 is the absolute value of the electron charge e. Notice that because the Hamiltonian is independent of $\hat{x}$ we can replace $\hat{k_x}$ with it's eigenvalue k_x. With these definitions in mind we rearrange Eq. 3.25

$$\begin{aligned}\frac{\epsilon_n^2}{8m\tilde{t}^2}\psi_n(y) = \Big(\frac{1}{2}m\omega^2(y-y_0)^2 + \frac{1}{2m}\hat{k_y}^2 - \frac{\omega}{2}\sin(2\alpha) - \\ \frac{\omega}{2}\cos(2\alpha)\{y-y_0, \hat{k_y}\}\Big)\psi_n(y).\end{aligned} \tag{3.27}$$

The solutions to this differential equation are of the form

$$\psi_n(y) = e^{im\omega\left(\frac{y^2}{2}-yy_0\right)e^{2i\alpha}}\Big(C_1 H_n(\sqrt{m\omega|\sin(2\alpha)|}(y-y_0))+ \\ C_2\ {}_1F_1(-\frac{n}{2};1/2;(m\omega|\sin(2\alpha)|(y-y_0)^2))\Big), \tag{3.28}$$

where $H_n(y)$ is the Hermite Polynomial of degree n and ${}_1F_1(-\frac{n}{2};1/2;y^2)$ is the Kummer confluent hypergeometric function. We find the energy eigenvalues of this system by requiring the index of the Hermite polynomials to be of integer value. Using this prescription we find

$$\epsilon_n = \pm\tilde{t}\sqrt{8|\sin(2\alpha)|m\omega n}, \tag{3.29}$$

or, in terms of the density wave condensation strength,

$$\epsilon_n = \pm 2\sqrt{\frac{e_0 B|W_0|t}{c}n}. \tag{3.30}$$

Solving Eq. 3.24 in the same fashion yields shifted levels

$$\epsilon_n = \pm 2\sqrt{\frac{e_0 B|W_0|t}{c}(n+1)}, \tag{3.31}$$

where $n = 0, 1, 2, 3, ...$ for both expressions. Due to the lack of the zero energy Landau level in Eq. 3.31 we see that the single particle wave functions will be nonzero only on the even sublattice for index $n = 0$, whereas wave functions will have nonzero amplitude on both even and odd sublattices for all $n > 0$.

Solving for the low energy behavior near the $(k_x, k_y) = (-\pi/2, -\pi/2)$ Dirac point yields the same eigenenergy expressions obtained for the $(\pi/2, \pi/2)$ case whereas we find the inverse of this even-odd behavior for the $(k_x, k_y) = (\pi/2, -\pi/2)$, $(-\pi/2, \pi/2)$ points. The Landau level expressions near these points can be obtained by flipping the signs in front of both of the $\cos(2\alpha)$, $\sin(2\alpha)$ terms in Eq. 3.27. In this case we find opposite wave function behavior–the single particle wave functions will be nonzero only on the odd sublattice for index $n = 0$, and wave functions will have nonzero amplitude on both odd and even sublattices for all $n > 0$.

From this analysis we see that for $W_0 \neq 0$ levels emerge from charge neutrality, regardless of the magnitude of W_0; this is due to the d-density wave's symmetry breaking nature. We plot characteristic Butterflies and the first few nonzero Landau levels according to Eq.s 3.30 and 3.31 in Fig.s 3.22 and 3.23.

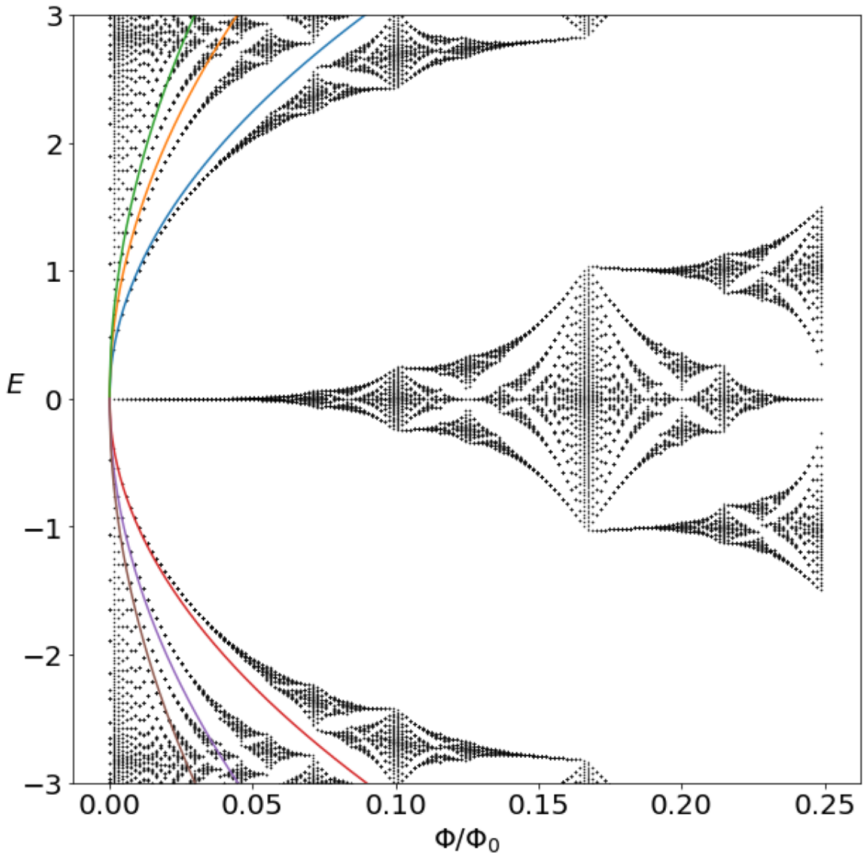

Figure 3.23: Plot of the butterfly and the associated first few nonzero Landau levels for $\alpha=\pi/4$.

CHAPTER 4

Density wave mediated Dzyaloshinskii-Moriya Interactions

This chapter is adapted from the publication:

Powell, I. E., Durr, S., Rombes, N. and Chakravarty, S. *Density Wave Mediated Dzyaloshinskii Moriya Interactions.*, Phys. Rev. B. **103**(2):024433, January 2021

4.1 Introduction

Despite concerted efforts to illuminate the precise nature of the pseudogap phase of the cuprate high-temperature superconductors[Var99, Var06, YRZ06, NPK07], it remains unclear which of a host of competing order parameters is responsible for the interesting behavior of this phase. One promising candidate[CLM01] is the $\ell = 2$ spin-singlet order, the d-density wave (DDW), which gives rise to a $d_{x^2-y^2}$ gap and currents that alternate between adjacent plaquettes on a square lattice. The relevance of this state is certainly believable given the proximity of the pseudogap phase to the antiferromagnetic Mott insulator at low doping, which doubles the Brillouin zone in the same way and is susceptible to singlet pairing.

This density wave state of nonzero angular momentum belongs to a larger class of such states[Nay00b], and it is worth exploring other, more exotic members of this class related to the singlet DDW which maintain the key characteristics necessary for relevance to the pseudogap phase. Such states are also of some interest due to their topological properties.[HRC11]

We focus on a mixed triplet-singlet DDW order, which has generated interest recently due to promising transport calculations consistent with surprising physics found in the pseudogap phase of the cuprate superconductor $La_{2-x}Sr_xCuO_4$ and related compounds.[GLB19, LL19] Namely, for nonzero hole doping, the mixed triplet-singlet DDW state generates a nonvanishing thermal Hall conductivity κ_{xy}, and hosts hole pockets on the reduced Brillouin zone boundaries consistent with Hall coefficient measurements.[CK08, DCL10]

At the mean-field level a general density wave state may be described by the Hamiltonian

$$H_{\mathrm{DW}} = \sum_{\mathbf{k},\mathbf{Q}} c^\dagger_{\mathbf{k}+\mathbf{Q}} [\Phi^\mu_{\mathbf{Q}}(\mathbf{k})\tau^\mu] c_{\mathbf{k}} + \mathrm{h.c.}, \tag{4.1}$$

where $c^\dagger_{\mathbf{k}}$, and $c_{\mathbf{k}}$ are the electron creation and annihilation operators at wave vector $\mathbf{k}$, $\mathbf{Q}$ is the wave vector at which the density wave condensation occurs, $\Phi^\mu_{\mathbf{Q}}(\mathbf{k})$ is proportional to an element of some representation of the space group of $\mathbf{Q}$ on the lattice, τ^1, τ^2, and τ^3 are the Pauli matrices, and $\tau^0 = \mathbb{1}$. This Hamiltonian can be thought of as arising from a mean-field decomposition of nearest neighbor electron-electron interaction terms in the most general problem[Lau14, NJK99, Sch89, KK03] in which the order parameter

$$\langle c^\dagger_{\mathbf{k}+\mathbf{Q},\alpha} c_{\mathbf{k},\beta} \rangle = [\Phi^\mu_{\mathbf{Q}}(\mathbf{k})\tau^\mu]_{\alpha\beta} \tag{4.2}$$

acquires a nonzero value for some nonzero $\mathbf{Q}$. In our work we assume that all terms which transform nontrivially under rotations and translations are captured by this mean-field decomposition.

Here we consider a specific example of Eq. (4.1), namely the the triplet-singlet DDW wave[HRC11] (denoted $i\sigma d_{x^2-y^2} + d_{xy}$)

$$\begin{aligned} \Phi^i_{\mathbf{Q}}(\mathbf{k}) &\propto iW_0 N_i (\cos k_x - \cos k_y) \\ \Phi^0_{\mathbf{Q}}(\mathbf{k}) &\propto \Delta_0 \sin k_x \sin k_y, \end{aligned} \tag{4.3}$$

where N_i is a unit vector pointing along the spin quantization direction, $i = 1, 2, 3$, and $\mathbf{Q} = (\pi/a, \pi/a)$. In real space the Hamiltonian is written as

$$H_{\mathrm{DDW}} = H_t + H_s \tag{4.4}$$

with

$$H_t = \frac{iW_0}{4}\sum_{i,\alpha,\beta}(-1)^{m+n}(\mathbf{N}\cdot\boldsymbol{\sigma})_{\alpha\beta} \times [c^\dagger_{i+a\hat{x},\alpha}c_{i,\beta} - c^\dagger_{i+a\hat{y},\alpha}c_{i,\beta}] + \text{h.c.} \tag{4.5}$$

and

$$H_s = \frac{\Delta_0}{4}\sum_{i,\alpha,\beta}\delta_{\alpha,\beta}(-1)^{m+n} \times \left[c^\dagger_{i+a\hat{x}+a\hat{y},\alpha}c_{i,\beta} - c^\dagger_{i+a\hat{x}-a\hat{y},\alpha}c_{i,\beta}\right] + \text{h.c.}. \tag{4.6}$$

The Hamiltonian $H_0 + H_{\text{DDW}}$, describes a topological Mott insulator[Nay00b, HRC11] with a quantized spin Hall conductance; it is a variant of the singlet d-density wave model hypothesized[CLM01] to explain the pseudogap phase of the cuprates. Unlike the singlet d-density wave state, however, the mixed triplet-singlet $i\sigma d_{x^2-y^2} + d_{xy}$-density wave state does not inherently break time reversal symmetry, yet it retains most of the signatures of the singlet d-density wave state. For example, the $i\sigma d_{x^2-y^2} + d_{xy}$-density wave wave state possesses hole pockets centered along the Brillouin zone diagonals which are consistent with both the measured Hall coefficient[GLB19] and some aspects of quantum oscillation experiments[DPL07, SHP08, WC16]. Recently, second-harmonic generation experiments have suggested that an inversion symmetry breaking is responsible for large second harmonic generation signatures in $YBa_2Cu_3O_y$[ZBL16] but we note that this could be due to, in principle, the quadrupole moment induced via a triplet d-density wave[Nay00b].

This model was shown by Z-X. Li & D-H. Lee to produce a nonzero thermal Hall effect away from half filling–however, despite considerable effort, we have not managed to exactly reproduce their plots using their parameter values and instead find a thermal Hall effect which is an order of magnitude smaller for nonzero temperatures shown here in Fig. 4.1. Details of the calculation are highlighted in the Appendix.

We now ask ourselves, what effect does this density wave state have on the pertinent magnetic physics near half filling? In our work we assume that at nonzero doping the density wave will survive in the presence of long range magnetic order[LL19]. The triplet

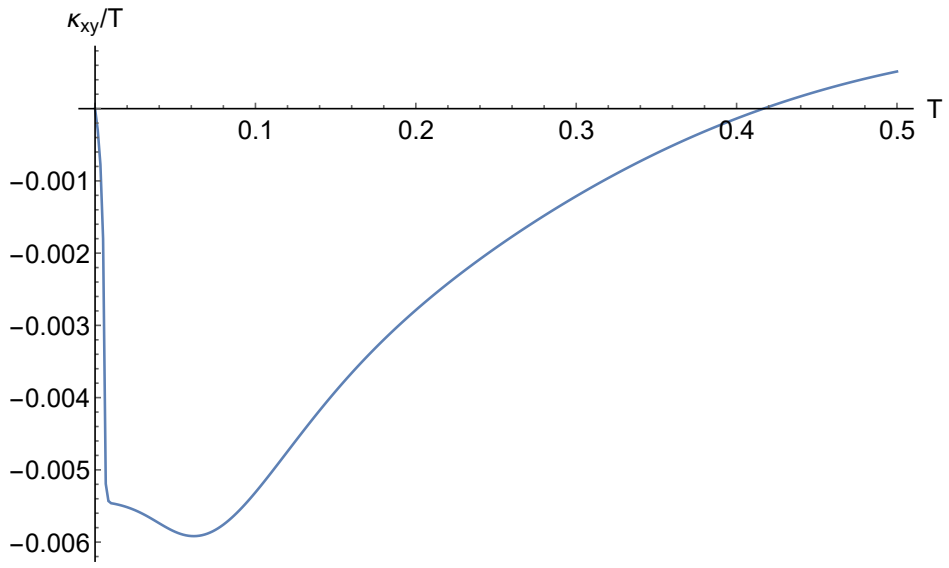

Figure 4.1: Thermal Hall conductivity κ_{xy}/T as a function of temperature T produced by the triplet-singlet DDW state defined by Equation (4.3) with $\Delta_0 = 0.3t$, magnetic field $B = 0.0075t/\mu_B$, $t' = -0.1t$, $W_0 = 2t$ at a doping of $p = 0.06$. κ_{xy} is listed here in units of $k_B^2/\hbar$.

part of the density wave order parameter induces a staggered spin current[NJK99] on the bonds of the lattice, and hence, for neighboring lattice points A and B, this intrinsic spin current implies that there exists no center of inversion at any point C on the bond connecting A and B, thereby allowing an antisymmetric exchange among the localized spins.[KKA16, Tat19] These types of (staggered) antisymmetric exchanges have been considered in the literature[KH19], but to our knowledge have never been considered in the context of being generated via the spin currents associated with density wave states. The spin currents intrinsic to the triplet flavored density wave states induce a Dzyaloshinskii-Moriya (DM) interaction between the underlying neighboring spins[KKA16], and we investigate the effect that this DM interaction has on antiferromagnetic and ferromagnetic spin textures, using a Holstein-Primakoff transformation expanded about the ground state. It has been previously demonstrated[SCS19, HPL19, KH19] that certain DM interactions can lead to a thermal Hall effect. We find that the particular DM interaction induced by triplet-singlet DDW states can not contribute to κ_{xy}, which is consistent with speculations on the nature of the neutral

excitation responsible for the sizable thermal Hall conductivity seen in the cuprates.[GLB19]

There are strong constraints and unique properties associated with the DM vectors that are generated by triplet density waves. Because triplet density wave states break spin-rotational invariance the associated Goldstone boson excitations will destroy the two dimensional triplet density wave order at finite temperatures unless there is some external mechanism which stabilizes the triplet density wave order parameter like interlayer coupling. However, we find that when the underlying band structure is sufficiently topologically nontrivial insofar as it hosts a nonzero spin Hall conductance, and an external magnetic field is turned on, the triplet density wave induced DM vectors are energetically stable in the absence of interlayer coupling. Furthermore, these DM vectors are pinned to be collinear with the magnetic field, regardless of its direction, and the DM interaction will have the same symmetry as the form factor of the triplet density wave.

In the following we derive the DM coefficients induced by triplet density waves and investigate the effects they have on the physics of the underlying spin textures of the lattice. We find that for a ferromagnetic background, the ground state remains perfectly collinear below some critical strength of the density wave; above the critical strength, the ground state acquires a nonzero canting angle, and we show that linear boson terms shift the classically-predicted threshold for nonzero canting angle. Assuming a small DM interaction the dispersion of the magnons in this case develop a characteristic $d_{x^2-y^2}$ gap. For an antiferromagnetic background we find that the density wave-induced DM interaction has a small effect unless there is some weak ferromagnetism present. We compute the spin-wave spectrum approptiate to LSCO and find that for modest density wave strengths there exists a small $d_{x^2-y^2}$ anisotropy.

4.2 The Effective Magnetic Hamiltonian

For any type of mixed triplet-singlet density wave condensation the mean-field Hamiltonian in the absence of on-site repulsion or ferromagnetic coupling can be written in the suggestive

manner

$$H = \sum_{ij} c^\dagger_{i\alpha}(t_{ij}\boldsymbol{\delta}_{\alpha,\beta} + i\boldsymbol{\lambda}_{ij}\cdot\boldsymbol{\sigma})c_{j\beta} \tag{4.7}$$

where all singlet density wave terms are absorbed into the definition of t_{ij}, and $\boldsymbol{\lambda}_{ij}$ are the triplet density wave terms which couple to $\boldsymbol{\sigma}$. It can be shown[KKM10, KKA16] that this $\boldsymbol{\lambda}_{ij}$ induces a DM interaction in the underlying spin structure (antiferromagnetic or ferromagnetic) whose coefficients are given by

$$\mathbf{D}_{ij} = \boldsymbol{\lambda}_{ij}\mathrm{Tr}_{\,\sigma} N_{ji}, \tag{4.8}$$

where $N_{ji} \equiv \langle c^\dagger_i c_j\rangle = -\frac{1}{\pi}\int_{-\infty}^{E_F} \mathrm{Im}\, G_{ji}(E)dE$, $G_{ji}(E)$ is the Green function defined by H, and E_F is the Fermi energy. Tracing the spin index over an expansion of $G_{ji}(E) = f(E)t_{ji}/t + g(E)\boldsymbol{\lambda}_{ji}\cdot\boldsymbol{\sigma}/t + \mathcal{O}(\lambda^2/t)$ reveals that to leading order $G_{ji}(E)$ should have the same symmetry as t_{ji} under translations and rotations. In this work we consider a specific example of Eq. (4.1), written in real space as

$$H_{\mathrm{DDW}} = H_0 + H_t + H_s \tag{4.9}$$

where H_0 is the tight binding Hamiltonian of the underlying crystal lattice which is some union of all square planar lattices which host the triplet-singlet-DDW. For this particular triplet-DDW case, because $\boldsymbol{\lambda}_{ij}$ only connects nearest neighbors, t_{ji} is simply the tight-binding kinetic energy coefficient which we will assume to transform trivially under rotation–thus we write

$$\mathbf{D}_{ij} = \alpha\boldsymbol{\lambda}_{ij} \tag{4.10}$$

for some constant α. Because we will allow the density wave strength to be a tunable parameter we will henceforth absorb α, and all other constant numerical prefactors into the definition of W_0. The DM coefficients for the triplet $d_{x^2-y^2}$-density wave therefore become

$$\begin{aligned} D^{\mathbf{N}}_{i,i\pm a\hat{x}} &= (-1)^{i_x+i_y}W_0 \\ D^{\mathbf{N}}_{i,i\pm a\hat{y}} &= -(-1)^{i_x+i_y}W_0, \end{aligned} \tag{4.11}$$

where $i = i_x + i_y$, and the superscript $\mathbf{N}$ denotes that the DM vector points along the $\mathbf{N}$ direction. We stress that the method implemented here can be applied, in general, to

triplet density waves in any angular momentum channel. The direction of the DM vector is along the triplet quantization axis, and the form factor associated with the triplet density wave dictates the symmetry of the DM vector on the lattice. To understand the order of magnitude of the DM interaction induced by density waves one can directly use Moriya's perturbation theory result (including the on-site repulsion U)[Mor60]

$$D \approx \frac{2tW_0}{U}, \tag{4.12}$$

which implies that a density wave-mediated DM interaction is roughly on the scale of 10-100 meV for LSCO at low doping for density wave stengths $W_0 \sim t$.

For a density wave-induced DM interaction to not be disordered by Goldstone modes at finite temperatures there must be some mechanism which externally stabilizes the triplet density wave's quantization axis, i.e. the direction of $\mathbf{N}$. Previously it was suggested that interlayer coupling was needed to stabilize the direction of $\mathbf{N}$[HRC11], however it was recently shown[LL19] that the direction of $\mathbf{N}$ for the triplet-singlet DDW in two dimensions can be stabilized by the bulk orbital magnetization's coupling to the magnetic field. Explicitly, a magnetic field induces a bulk orbital magnetization, M, which is given by[CTV06]

$$M = -\sum_{\alpha=\mathbf{N}\cdot\boldsymbol{\sigma}=\pm 1} \frac{e}{hc} C_\alpha \Delta E_{Z,\alpha}, \tag{4.13}$$

where C_α is the Chern number of the band of spin α, e is the electron charge h is Planck's constant, c is the speed of light, and $\Delta E_{Z,\alpha}$ is the Zeeman splitting

$$\Delta E_{Z,\alpha} = -\alpha \mu_B \mathrm{sgn}(W_0) \mathbf{N} \cdot \mathbf{B}, \tag{4.14}$$

where μ_B is the Bohr magneton. For the case of the triplet-singlet DDW the resulting energy density due to the orbital magnetization-magnetic field is[LL19]

$$\Delta \mathcal{E}_{\text{Zeeman}} = -\frac{\mu_B B^2}{\pi c} \mathrm{sgn}(W_0 \Delta_0)(\mathbf{N} \cdot \hat{\mathbf{B}}), \tag{4.15}$$

which implies that it is energetically most favorable for $W_0 \Delta_0 \mathbf{N} \parallel \mathbf{B}$. Thus, for $\Delta_0 > 0$, $\mathbf{B} \neq 0$, Eq. 4.11 necessarily becomes

$$\begin{aligned} D^{\mathbf{B}}_{i,i\pm a\hat{x}} &= (-1)^{i_x+i_y}|W_0| \\ D^{\mathbf{B}}_{i,i\pm a\hat{y}} &= -(-1)^{i_x+i_y}|W_0|. \end{aligned} \tag{4.16}$$

From this argument alone we see that stable density wave-induced DM interactions in two dimensions can only arise from topological density waves with nonvanishing spin Hall conductance–that is, given $\Delta E_{Z,+1} = -\Delta E_{Z,-1}$, stability is only guarenteed if $C_{+1} = -C_{-1}$. Furthermore, because density wave-induced DM vectors must be collinear with the magnetic field, they will transform like the magnetic field under rotations and time-reversal. This immediately implies that the corresponding magnons in the problem will have no contribution to any thermal Hall effect because of the spin rotation and time-reversal symmetry considerations outlined by R. Samajdar et. al.[SCS19]

$$\begin{aligned} \kappa_{xy}[J, \mathbf{D}_{ij}, \mathbf{B}] &= \kappa_{xy}[J, R_{\boldsymbol{\phi}}\hat{\mathbf{B}} D_{ij}, R_{\boldsymbol{\phi}}\mathbf{B}] \\ \kappa_{xy}[J, \mathbf{D}_{ij}, \mathbf{B}] &= -\kappa_{xy}[J, -\hat{\mathbf{B}} D_{ij}, -\mathbf{B}], \end{aligned} \tag{4.17}$$

where $R_{\boldsymbol{\phi}}$ is the vector representation of spin rotation by some angle ϕ about the axis defined by $\hat{\boldsymbol{\phi}}$. Rotating the system about an angle π about an axis perpendicular to $\hat{\mathbf{B}}$ maps $R_{\boldsymbol{\phi}}\hat{\mathbf{B}}$ to $-\hat{\mathbf{B}}$ and hence $\kappa_{xy} = -\kappa_{xy} = 0$. The bulk magnetization (Eq. 4.13) would, in principle, produce a small ferromagnetic-like signal detectable in polar Kerr measurements so long as the external magnetic field is not exactly zero for weak disorder at small enough temperatures. More detailed calculations involving interlayer coupling, the inclusion of magnetic impurities, and nonzero temperatures should be considered in future work to quantitatively compare this triplet-singlet DDW bulk magnetization signal to the polar Kerr rotation data previously gathered[XSD08]. Interesting questions to ask are how the Goldstone modes would disorder the DM vectors in the absence of an external magnetic field, and how the DM vectors behave for density wave states with vanishing spin Hall conductances.

We now study the effect of this dynamically generated DM interaction on the isotropic two dimensional Heisenberg ferromagnet and antiferromagnet. Namely, we consider

$$H = \pm J \sum_{i,j} \mathbf{S}_i \cdot \mathbf{S}_j + \sum_{i,j} \mathbf{D}_{ij} \cdot (\mathbf{S}_i \times \mathbf{S}_j) - \mathbf{B} \cdot \sum_i \mathbf{S}_i, \tag{4.18}$$

where J is the absolute value of the spin exchange, the $\pm$ corresponds to the antiferromagnetic or ferromagnetic cases respectively, and the DM interaction includes the contribution from the density wave.

4.3 The Antiferromagnetic Background

The triplet-singlet density wave induced DM interaction will typically have little effect on perfectly antiferromagnetic backgrounds in the linear spin wave approximation. This is because, upon turning on a magnetic field to stabilize the DM interaction, the localized spins will flop perpendicular to the magnetic field direction. Terms which couple to W_0 in this case are proportional to higher order terms in the HP bosons. When this happens only very large density wave strengths will cause distortions in the magnetic ordering. On the other hand, if there exists some small ferromagnetic component associated with the otherwise antiferromagnetic ordering, the density wave-induced DM interaction appears in terms quadratic in the HP bosons and thus will affect the magnon dispersion. This is the case for LSCO which we will consider in the following.

Taking $\mathbf{B} = B\hat{z}$ the DM matrix for LSCO can be written [CTF89, CRZ91, TA94] as $\mathbf{D}_{ij} = (-1)^{i_x+i_y}\mathbf{D}$, where

$$\mathbf{D} = \begin{pmatrix} \sqrt{2}D\cos\theta_d & \sqrt{2}D\sin\theta_d & W_0 \\ -\sqrt{2}D\sin\theta_d & -\sqrt{2}D\cos\theta_d & -W_0 \\ 0 & 0 & 0 \end{pmatrix}. \tag{4.19}$$

The x and y spin direction entries are due to the buckling of the oxygen atoms out of the copper oxide plane and induce a weak net ferromagnetic moment out of the copper oxide plane. The z spin direction entries come from Eq. (4.16) where we have assumed a nonzero density wave strength $\propto W_0$. We find the mean-field ground state by summing the classical energy over the two sublattices and then numerically minimizing this energy with respect to the two sets of spherical angles which characterize the classical spin directions. Here we parameterize the spins as

$$\langle \mathbf{n}_i \rangle = (\cos\phi_i, \sin\phi_i, n_z) \tag{4.20}$$

where n_z is the weak ferromagnetic canting due to D. For density wave strengths on the order of t the ground state is unchanged–characterized by antiferromagnetic spin flopping in the plane perpendicular to the magnetic field with a weakly ferromagnetic component

pointing along B induced by D. Closely following the work of Han, Park, and Lee[HPL19], we choose the form of the classical ground state as

$$\langle \bar{\mathbf{n}}_i \rangle = -\frac{(-1)^{i_x+i_y}}{\sqrt{2}} \cos\theta_c(\hat{x}+\hat{y}) + \sin\theta_c \hat{z}. \tag{4.21}$$

We expand our spin operators about this mean-field ground state[HF09]

$$\mathbf{S}_i = a_i \langle \mathbf{n}_i \rangle + \mathbf{t}_i \tag{4.22}$$

so that we can perform the appropriate Holstein-Primakoff (HP) substitution. The amplitudinal reduction along the mean-field state is given as

$$a_i = S - b_i^\dagger b_i, \tag{4.23}$$

and, to leading order in boson density operators, the transverse fluctuation operator $\mathbf{t}_i$ is given by

$$\mathbf{t}_i = t_i^{x'} \hat{x}_i' + t_i^{y'} \hat{y}_i', \tag{4.24}$$

with

$$\begin{aligned} t_i^{x'} &= \sqrt{\frac{S}{2}}(b_i^\dagger + b_i) \\ t_i^{y'} &= i\sqrt{\frac{S}{2}}(b_i^\dagger - b_i) \end{aligned} \tag{4.25}$$

where the primed coordinates are defined such that $\hat{x_i'} \times \hat{y_i'} = \langle \mathbf{n}_i \rangle$. Upon substitution of these operators into the antiferromagnetic version of Eq. (4.18) the terms quadratic in Boson creation and annihilation operators in the Hamiltonian can be written in real space as (redefining the couplings to absorb S)

$$\begin{aligned} H = (4J' + B\sin(\theta_c)) \sum_i b_i^\dagger b_i - \sum_{\langle i,j \rangle} J t_i^{x'} t_j^{x'} + J' t_i^{y'} t_j^{y'} \\ + \sum_i D'[t_i^{x'} t_{i+x}^{y'} + t_i^{y'} t_{i+x}^{x'} - t_i^{x'} t_{i+y}^{y'} + t_i^{y'} t_{i+y}^{x'}] \\ + i \sum i W_0 (-1)^{i_x+i_y} [b_i b_j^\dagger - b_i^\dagger b_j], \end{aligned} \tag{4.26}$$

where $J' = J/\cos(2\theta_c)$ and $D' = \cos(\theta_c) D(\cos\theta_d + \sin\theta_d)$. We take the Fourier transformation and write our Hamiltonian in Nambu form as

$$H = \sum_k \frac{1}{2} \psi_k^\dagger \mathcal{H}_k \psi_k \tag{4.27}$$

where $\psi_k^\dagger = (b_k^\dagger, b_{k+Q}^\dagger, b_{-k}, b_{-k+Q})$ and

$$\mathcal{H}_k = \begin{pmatrix} A_k & 2iW_k\sin\theta_c & B_k & 0 \\ 0 & -A_k & 0 & -B_k \\ 0 & 0 & A_k & -2iW_k\sin\theta_c \\ 0 & 0 & 0 & -A_k \end{pmatrix} + \text{h.c.}, \tag{4.28}$$

where

$$\begin{aligned} A_k &= 2J' + \frac{B}{2}\sin\theta_c + \frac{1}{2}(J'-J)(\cos k_x + \cos k_y) \\ B_k &= -2iD'(\cos k_x - \cos k_y), \\ &\quad - (J'+J)(\cos k_x + \cos k_y), \\ W_k &= W_0(\cos k_x - \cos k_y). \end{aligned} \tag{4.29}$$

The spectrum is given by the absolute value of the eigenvalues of the dynamic matrix[Col78] $K = (\sigma_3 \otimes \mathbb{I}_2)\mathcal{H}_k$– these eigenvalues correspond to what are called particle and hole bands for the positive and negative eigenvalues respectively. We plot the dispersion in Fig. 4.2 for a set of parameter values. Taking into account both the particle and hole bands the dispersion consists of one four-fold degenerate magnon branch very similar to that which is obtained when $W_0 = 0$; because W_0 couples to the weak ferromagnetic moment its effects on the spectrum are small if the density wave strength is not very large. Namely, tuning W_0 from zero induces a weak anisotropy in the the magnon dispersion along the k_x and k_y directions. The dispersion along $k_d = k_x = k_y$ is unchanged by increasing W_0 whereas the energy is increased along the $\mathbf{k} = (k_x, 0)$, $\mathbf{k} = (0, k_y)$ directions. This anisotropy is demonstrated in Fig. 4.3, where the largest deviation from the unperturbed magnon dispersion is roughly 0.4 meV when $k = (0, \pi)$ and $k = (\pi, 0)$. The thermal Hall conductivity is given by [MSM14]

$$\frac{\kappa_{xy}}{T} = -\sum_n \frac{k_B^2}{\hbar}\int \frac{1}{(2\pi)^2}\left[c_2(n_B(\omega_{n,\mathbf{k}})) - \frac{\pi^2}{3}\right]\Omega_n^z(\mathbf{k}) \tag{4.30}$$

where

$$c_2(x) = \int_0^x ds\left(\ln\left[\frac{1+s}{s}\right]\right)^2, \tag{4.31}$$

n_B is the Bose distribution function, Ω_n^z is the Berry curvature of the nth band, and the sum is taken over the particle bands. Because the particle band in this model is twofold

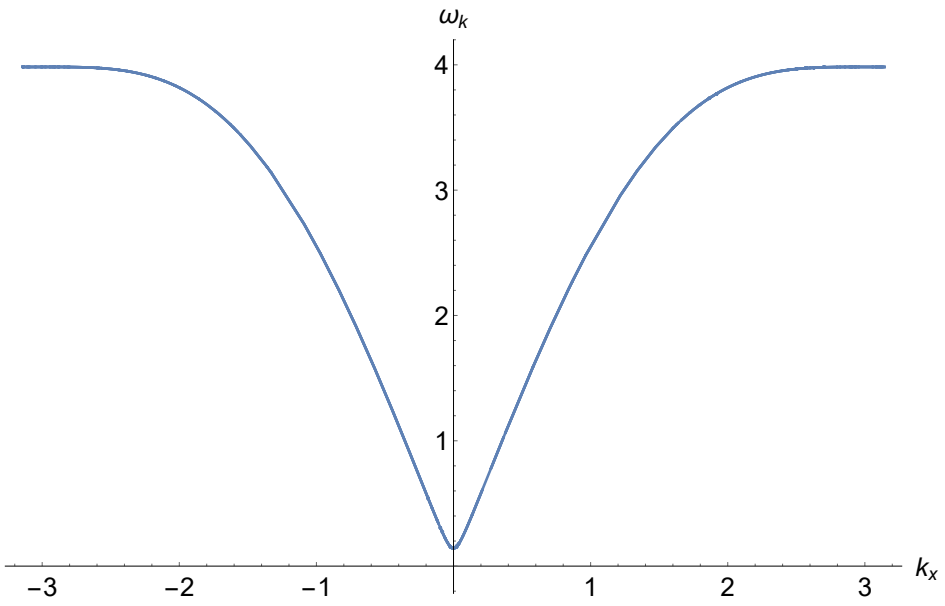

Figure 4.2: Magnon dispersion ω_k for $k_y = 0$ in units of J for $W_0 = 0.3J$, $D = 0.1J$, $\theta_d = 0.05$, $B = 0.05J$. The spectrum remains antiferromagnetic with small corrections increasing with the value of k_x.

degenerate we calculate its non-abelian Berry curvature using the discretized link method [FHS05] We define the Berry curvature as

$$\Omega^z(\mathbf{k}) = -i\ln[\tilde{U}_1(\mathbf{k})\tilde{U}_2(\mathbf{k}+\mathbf{e}_1)\tilde{U}_1(\mathbf{k}+\mathbf{e}_2)^{-1}\tilde{U}_2(\mathbf{k})^{-1}] \tag{4.32}$$

where the vectors $\mathbf{e}_1 = 2\pi(1,0)/N$, $\mathbf{e}_2 = 2\pi(0,1)/N$, and N^2 is the total number of lattice sites. The link variables are defined as

$$\tilde{U}_\gamma(\mathbf{k}) = \frac{\det U_\gamma(\mathbf{k})}{|\det U_\gamma(\mathbf{k})|} \tag{4.33}$$

where the matrix entries of $U_\gamma(\mathbf{k})$ are the eigenstate overlap elements in the degenerate subspace, which for the magnon case take the form [SMM13]

$$U_\gamma(\mathbf{k}) = \begin{pmatrix} \langle\psi_1(\mathbf{k})|\tilde{\psi}_1(\mathbf{k}+\mathbf{e}_\gamma)\rangle & \langle\psi_1(\mathbf{k})|\tilde{\psi}_2(\mathbf{k}+\mathbf{e}_\gamma)\rangle \\ \langle\psi_2(\mathbf{k})|\tilde{\psi}_1(\mathbf{k}+\mathbf{e}_\gamma)\rangle & \langle\psi_2(\mathbf{k})|\tilde{\psi}_2(\mathbf{k}+\mathbf{e}_\gamma)\rangle \end{pmatrix}. \tag{4.34}$$

Here the magnon eigenstates $|\psi_i(\mathbf{k})\rangle$ are the normalized eigenvectors of K that correspond to the positive energy eigenvalues–i.e. the particle bands, and $|\tilde{\psi}_i\rangle = (\sigma_3 \otimes \mathbb{I}_2)|\psi_i\rangle$. We

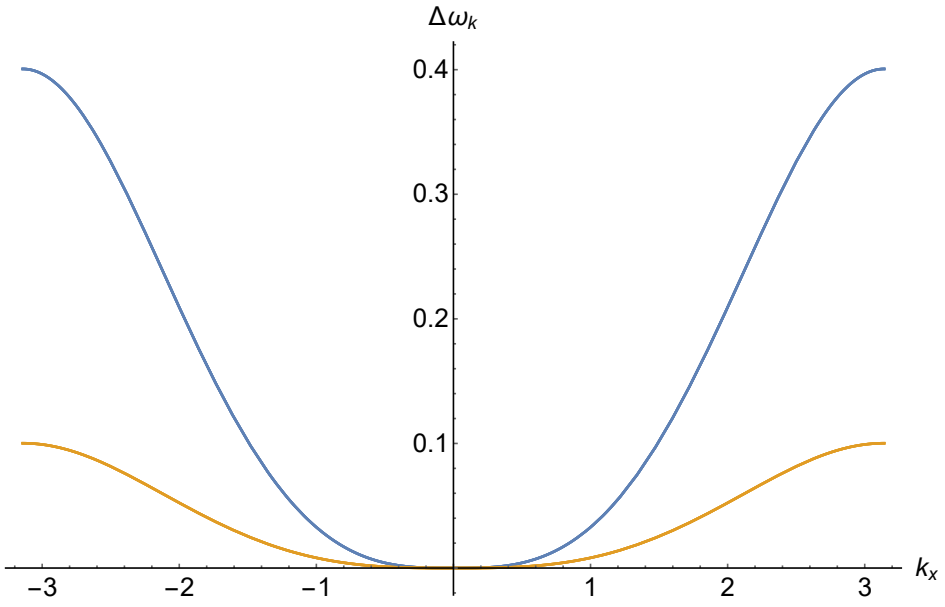

Figure 4.3: The difference in the magnon dispersions listed in meV with $k_y = 0$, $D = 12$ meV, $\theta_d = 0.05$, and $B = 6$ meV. The orange, and blue curves correspond to the difference between the $W_0 = 100$ meV and $W_0 = 0$ dispersions and the difference between the $W_0 = 50$ meV and $W_0 = 0$ dispersions respectively.

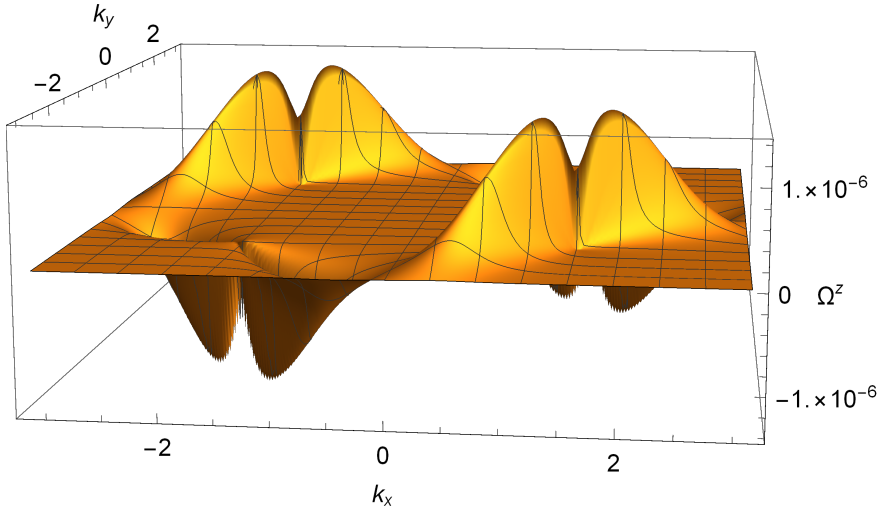

Figure 4.4: Non-abelian Berry curvature calculated on a 200×200 lattice with $W_0 = 0.3J$, $D = 0.1J$, $\theta_d = 0.05$, $B = 0.05J$.

plot the non-abelian Berry curvature calculated on an 200×200 lattice in Fig. 4.4 for a characteristic set of parameter values. Assuming that Eq. (4.30) can be generalized trivially for the case of non-abelian Berry curvature for a twofold degenerate magnon branch it can be seen immediately that $\kappa_{xy} = 0$ because our numerically calculated $\Omega^z(\mathbf{k})$ obeys $\Omega^z(k_x, k_y) =$ -$\Omega^z(-k_x, k_y)$ = -$\Omega^z(k_x, -k_y)$ whereas $\omega(k_x, k_y) = \omega(-k_x, k_y) = \omega(k_x, -k_y)$–thereby causing the integral to vanish.

4.4 The Ferromagnetic Background

It has previously been shown[KK03] via a one-loop renormalization group analysis of the extended U-V-J model that triplet $d_{x^2-y^2}$-density wave condensation is energetically favorable for a range of interaction strengths given $J/U < 0$. Furthermore, it was theoretically predicted[KGC07] and recently experimentally confirmed[SWZ20] that the highly overdoped cuprates show ferromagnetic ordering in the CuO_2 planes. Due to these reasons we investigate the mixed triplet-singlet density wave DM interaction effects on a two-dimensional Heisenberg ferromagnet. Taking $\mathbf{B} = B\hat{z}$ the symmetric exchange term favors mean-field states of the form

$$\langle \bar{\mathbf{S}}_i \rangle = n_z \hat{z}, \tag{4.35}$$

and the antisymmetric exchange favors mean-field states of the form

$$\begin{aligned} \langle \tilde{\mathbf{S}}_i \rangle &= \xi_x(\mathbf{r}_{i_x,i_y})\hat{x} + \xi_y(\mathbf{r}_{i_x,i_y})\hat{y}, \\ \xi_x(\mathbf{r}_i) &= \xi_0 \frac{[(-1)^{i_x} + (-1)^{i_y}]}{2} \\ \xi_y(\mathbf{r}_i) &= \xi_0 \frac{[(-1)^{i_x} - (-1)^{i_y}]}{2}. \end{aligned} \tag{4.36}$$

Thus, the mean-field state which occurs in the presence of both types of exchange is

$$\langle \mathbf{n}_i \rangle = \langle \bar{\mathbf{S}}_{i_x,i_y} \rangle + \langle \tilde{\mathbf{S}}_{i_x,i_y} \rangle. \tag{4.37}$$

We have checked that this is the true mean-field ground state by summing the classical energy over the four sublattices and then numerically minimizing the energy with respect

to the four sets of spherical angles which characterize the classical spin directions. The mean-field energy per site in this case is (restoring S)

$$\begin{aligned}\frac{E_0}{N} = &-|J|zS^2\cos^2(\theta)/2 - 2S^2|W_0|\sin^2(\theta) \\ &- BS\cos(\theta),\end{aligned} \tag{4.38}$$

where N is the number of lattice sites, $z = 4$ (6) in two (three) dimensions, and θ is defined as the angle between $\langle \bar{\mathbf{S}}_{i_x,i_y} \rangle$ and $\langle \mathbf{n}_i \rangle$. For the square lattice case the ground state is minimized about $\theta = 0$ for all $2W_0 < z|J|/2 + B/S$, whereas the ground state is minimized at $\theta = \cos^{-1}[B/(4S(W_0 - J))]$ for $2W_0 > z|J|/2 + B/S$.

Following the procedure highlighted in the previous section we expand the operators about the mean-field ground state, Eq. (4.37), and substitute them into the ferromagnetic version of Eq. (4.18) to yield the real space Hamiltonian

$$H = E_0 + H_0 + H', \tag{4.39}$$

where the classical mean field energy E_0 is defined in Eq. (4.38), H_0 is

$$\begin{aligned}H_0 = \sum_i \mu b_i^\dagger b_i + \sum_{\langle i,j \rangle} [&\bar{Z}_\theta g(j) b_i^\dagger b_j + \tilde{Z}_\theta g(j) b_i^\dagger b_j^\dagger \\ &+ iJS\cos(\theta)(-1)^{i_x+i_y} b_i b_j^\dagger + \text{h.c.}],\end{aligned} \tag{4.40}$$

with $g(j) = +1$ for $j = i + \hat{x}$, and $g(j) = -1$ for $j = i + \hat{y}$, and the coefficients are defined as

$$\begin{aligned}\bar{Z}_\theta &\equiv \frac{JS}{2}\sin^2(\theta) + \frac{W_0 S}{2}(\cos^2(\theta) + 1) \\ \tilde{Z}_\theta &\equiv \frac{JS}{2}\sin^2(\theta) + \frac{W_0 S}{2}(\cos^2(\theta) - 1) \\ \mu &\equiv 4JS\cos^2(\theta) + 4W_0 S\sin^2(\theta) + B\cos(\theta),\end{aligned} \tag{4.41}$$

and H' is

$$H' = \sum_i (-1)^{i_x} A_\theta (b_i^\dagger + b_i), \tag{4.42}$$

where

$$A_\theta = \sin(\theta)\left[\sqrt{\frac{S}{2}}B + \left(J(2S)^{3/2} - W_0(2S)^{3/2}\right)\cos(\theta)\right]. \tag{4.43}$$

Terms linear in boson creation and annihilation operators imply spin-wave creation and annihilation from the ground state. Thus, assuming that the system is in its ground state, it is typically argued in the literature that this coefficient A_θ must vanish at each point i on the lattice; in the following we show that allowing small A_θ has a nontrivial effect on the critical behavior of the system.

There exist two unique solutions for vanishing A_θ: the perfectly ferromagnetic case of $\theta = 0$, and

$$|\theta| = \cos^{-1}\left[\frac{B}{4S(W_0 - J)}\right] \tag{4.44}$$

which is the aforementioned magnetic ground state canting angle that occurs at the classical mean-field level when $2W_0 > 2J + B/S$. Anticipating quantum corrections to the ground state canting angle we opt to include the effects of $A_\theta \neq 0$–however, to maintain consistency with the Holstein-Primakoff substitution about the mean-field ground state it is understood that A_θ is necessarily either small or exactly zero, i.e. we are expanding sufficiently close to the classical mean-field theory's predicted relationship between the parameters. Thus, instead of taking $A_\theta = 0$, we eliminate terms linear in bosonic creation and annihilation operators by performing the canonical transformation

$$\begin{aligned} b_i &= \tilde{b_i} - (-1)^{i_x} x \\ b_i^\dagger &= \tilde{b}_i^\dagger - (-1)^{i_x} x, \end{aligned} \tag{4.45}$$

where x is the C-number

$$x = \frac{-A_\theta}{4\bar{Z}_\theta + 4\tilde{Z}_\theta - \mu}. \tag{4.46}$$

Note that this transformation is well defined when the denominator $4\bar{Z}_\theta + 4\tilde{Z}_\theta - \mu \neq 0$–this is indeed the case when we investigate the physics in close proximity to the mean-field behavior. The Hamiltonian then becomes

$$H = E_0 - NxA_\theta + H_0' = E_0' + H_0', \tag{4.47}$$

where H_0' is identical to the Hamiltonian written in Eq. (4.40) but in terms of the transformed bosonic operators $\tilde{b}_i$. Upon Fourier transformation the total Hamiltonian can be written in

terms of the Nambu basis as

$$H = E_0'' - NxA_\theta + \sum_k \frac{1}{2}\psi_k^\dagger \mathcal{H}_k \psi_k \tag{4.48}$$

where $\psi_k^\dagger = (\tilde{b}_k^\dagger, \tilde{b}_{k+Q}^\dagger, \tilde{b}_{-k}, \tilde{b}_{-k+Q})$,

$$\mathcal{H}_k = \begin{pmatrix} \bar{Z}_{\theta,k} + \mu/2 & iJ_k\cos(\theta) & 2\tilde{Z}_{\theta,k} & 0 \\ 0 & -\bar{Z}_{\theta,k} + \mu/2 & 0 & -2\tilde{Z}_{\theta,k} \\ 0 & 0 & \bar{Z}_{\theta,k} + \mu/2 & -iJ_k\cos(\theta) \\ 0 & 0 & 0 & -\bar{Z}_{\theta,k} + \mu/2 \end{pmatrix} + \text{h.c.}, \tag{4.49}$$

$$\begin{aligned} \frac{E_0''}{N} = &-2S(S+1)[J\cos^2(\theta) + |W_0|\sin^2(\theta)] \\ &- B(S+1/2)\cos(\theta), \end{aligned} \tag{4.50}$$

and $\bar{Z}_{\theta,k} = \bar{Z}_\theta[\cos k_x - \cos k_y]/2$, $\tilde{Z}_{\theta,k} = \tilde{Z}_\theta[\cos k_x - \cos k_y]$, $J_k = JS[\cos k_x + \cos k_y]$.

The spectrum is given by the absolute value of the eigenvalues of the dynamic matrix[Col78] $K = (\sigma_3 \otimes \mathbb{I}_2)\mathcal{H}_k$. The Hamiltonian, written in terms of the appropriate Bogoliubov operators γ_k, is then

$$H = E_g + \sum_{k,n} \omega_{k,n} \gamma_{k,n}^\dagger \gamma_{k,n}, \tag{4.51}$$

where n is the band index and the ground state energy E_g is

$$E_g = E_0'' - NxA_\theta + \sum_{k,n} \frac{\omega_{k,n}}{2}. \tag{4.52}$$

The canting angle is now determined by minimizing E_g with respect to θ. The effects of the linear boson terms can be seen by comparing the critical value of W_0^* obtained by E_0'' and by $E_0'' - NxA_\theta$ in the absence of quantum corrections. Upon expanding E_0'' to leading order in θ we yield (setting $S = 1/2$)

$$E_0''(\theta)/N \approx -\frac{3J}{2} - B + \left[\frac{B}{2} + \frac{3J}{2} - \frac{3W_0}{2}\right]\theta^2, \tag{4.53}$$

whereas the expansion of $E_0''/N - xA_\theta$ is

$$E_0''(\theta)/N - xA_\theta \approx -\frac{3J}{2} - B + \left[\frac{B}{4} + J - W_0\right]\theta^2. \tag{4.54}$$

The critical value of W_0^* can be obtained by finding its value when the θ^2 coefficient changes sign. Hence, without linear boson effects $W_0^* = J + B/3$, whereas including the linear boson effects reduces the critical value to $W_0^* = J + B/4$. This technique can be applied to general noncollinear spin systems to identify shifts in critical values of the parameters in the theory.

The dispersion for modest values of W_0 consists of two two-fold degenerate branches with a characteristic $d_{x^2-y^2}$ gap–this is due to the translation symmetry breaking nature of the DM interaction. For higher period incommensurate triplet density wave states the number of magnon branches will be equal to the period of incommensurability because it is precicely that period which determines the number of sites contained per unit cell. For $\theta = 0$ and $S = 1/2$ the magnon dispersion is

$$\omega_{k,n} = \frac{1}{2}B + J \pm \frac{1}{2}\sqrt{J^2(\cos k_x + \cos k_y)^2 + W_0^2(\cos k_x - \cos k_y)^2} \tag{4.55}$$

where the $\pm$ corresponds to the upper and lower band respectively. The dispersion is plotted along the high symmetry directions for some representative values of B, W_0, θ in Figs. 5-8. As W_0 is tuned from zero the low energy physics is govened by the $k = (0, 0)$ point and gaps develop at $k = (\pi, 0)$, $k = (0, \pi)$ with an energy difference of $2W_0$. As W_0 approaches its critical value the lowest energy excitations are goverend by $k = (0, 0)$, $k = (\pi, 0)$, $k = (0, \pi)$. Tuning W_0 beyond the critical value of density wave strength the low energy excitations are described entirely by the points $k = (\pi, 0)$, $k = (0, \pi)$, and the spectrum is shifted upwards in energy due to the canting of the localized moments.

4.5 Discussion

Through the effect that density waves have on the localized spins of a square lattice in a magnetically ordered phase, we find that the mixed triplet-singlet d-density wave state induces *stable* Dzyaloshinskii-Moriya (DM) interactions among the localized spins in the presence of an external magnetic field. The density wave-mediated DM vector is stabilized in topological systems by the direction of the magnetic field, and the symmetry such a

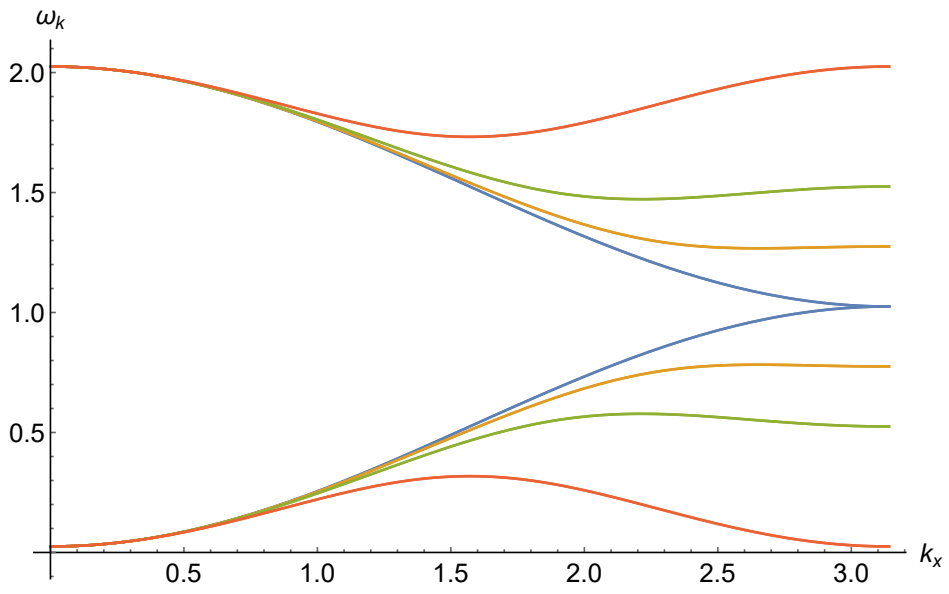

Figure 4.5: Magnon dispersion ω_k with $k_y = 0$ in units of J for various values of density wave strength with $B = 0.05J$. The blue, orange, green, and red curves correspond to $W_0 \to 0$, $W_0 = 0.25J$, and $W_0 = 0.5J$, $W_0 = J$ respectively, all below W_0^*. As W_0 is increased the gap at $k = (\pi, 0)$ increases as $2W_0$.

DMI is governed entirely by the angular momentum channel of the triplet density wave. Although it has been shown that the triplet-singlet density wave state produces a nonzero thermal Hall effect[LL19], the magnitude of the experimentally-measured thermal Hall effect exceeds the maximum possible contribution from the density wave state alone by an order of magnitude. The excitations of a spin system including DM interactions can, in principle, contribute to the thermal Hall conductivity[SCS19, HPL19, KH19]; however, we have shown the particular form of DM interaction generated by the triplet density wave does not seem to produce a nonzero κ_{xy}, and thus no additional contribution can be found through the influence of the density wave state on the underlying spin system. Triplet-singlet density wave order is notoriously difficult to detect directly[HRC11], and so it is important to explore possible influences that the state might have on its host system. Experimental detection of such features could, for example, help to assess the importance of the triplet-singlet DDW state in the description of the pseudogap phase of the cuprates. The magnetic structure of

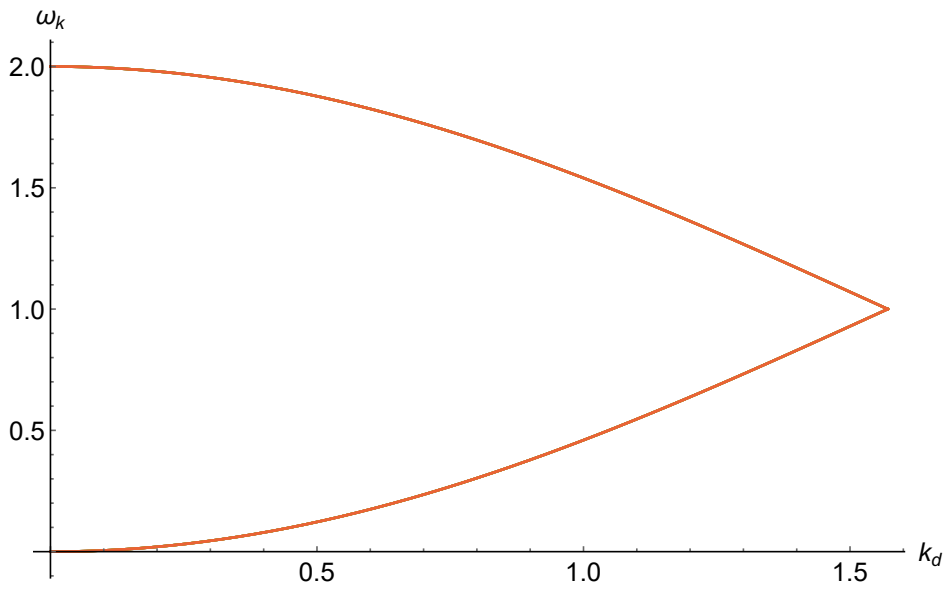

Figure 4.6: Magnon dispersion ω_k along the line $k_x = k_y = k_d$ in units of J for various values of density wave strength with $B = 0.05J$. Tuning W_0 does not alter the dispersion in this direction.

LSCO at low doping is Neel order with a small ferromagnetic moment. We have shown that in such a system, the presence of the DDW induces anisotropy in the spin-wave dispersion, reflecting the anisotropy of the DDW. Furthermore, the magnon branch for such a system has a non-abelian berry curvature that vanishes upon integration in such a way that $\kappa_{xy} = 0$.

Additionally, a two patch RG analysis of the U-V-J model indicates that triplet $d_{x^2-y^2}$-density wave order is can be energetically favorable in a finite region of coupling space given $J/U < 0$.[KK03] Ferromagnetic ordering was also predicted[KGC07] to emerge in the highly overdoped cuprates and experimentally confirmed[SWZ20] to exist in the CuO_2 planes of the cuprates. We find that the $i\sigma d_{x^2-y^2} + d_{xy}$-density wave-induced DM interaction in a 2D ferromagnetic system generically produces a magnon spectrum with two branches with a characteristic $d_{x^2-y^2}$ gap. For higher period incommensurate triplet density wave states in such a spin system the number of magnon branches is equal to the density wave's period of incommensurability.

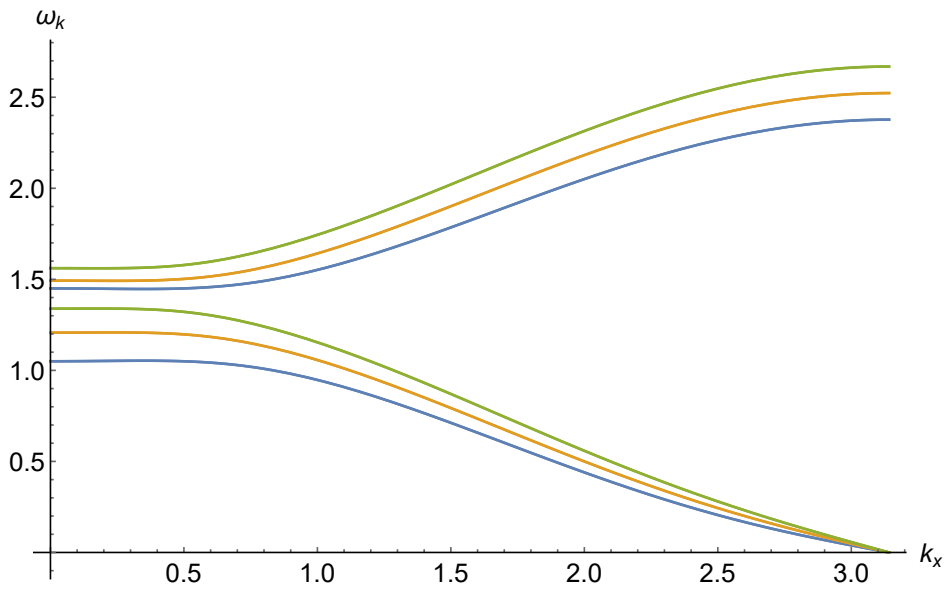

Figure 4.7: Magnon dispersion ω_k with $k_y = 0$ in units of J for various values of density wave strength with $B = 0.1J$ with the appropriate canting angles determined by minimization of Eq. (4.52) The blue, orange, and green curves correspond to $W_0 \to 1.25J$, $W_0 = 1.35J$, and $W_0 = 1.45J$ respectively, all above W_0^*. As W_0 is increased the gap at $k = (\pi, 0)$ increases as $2W_0$. The low energy excitations are now governed solely by the points $k = (0, \pi)$ and $(\pi, 0)$.

We have also found that the inclusion of terms in the Hamiltonian linear in Holstein-Primakoff boson operators has a nontrivial effect on the critical behavior of the Hamiltonian. These terms are typically ignored in the literature, which is justified when considering models that are far from the critical regime; however, we have shown that they induce shifts in the critical parameter values which control collinear to noncollinear phase transitions.

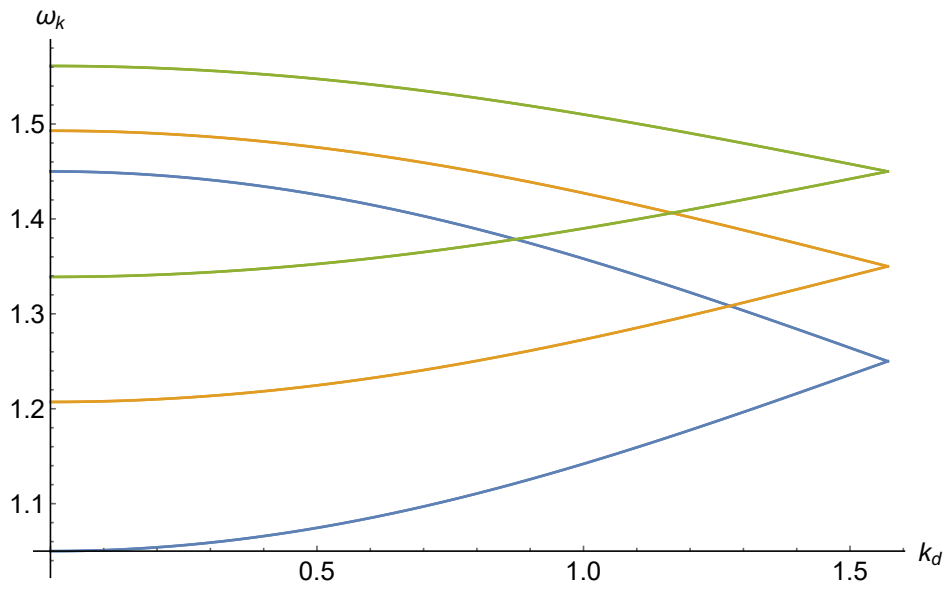

Figure 4.8: Magnon dispersion ω_k along the line $k_x = k_y = k_d$ in units of J with $B = 0.1J$ with the appropriate canting angles determined by minimization of Eq. (4.52). The blue, orange, and green curves correspond to $W_0 \to 1.25J$, $W_0 = 1.35J$, and $W_0 = 1.45J$ respectively, all above W_0^*. Nonzero canting shifts the spectrum upwards in energy.

4.6 Appendix: Calculating the thermal Hall coefficient

In our calculation we compute κ_{xy} using the Mott-like formula [WZ09, QNS11, QZS12, MM11, MSM14]

$$\frac{\kappa_{xy}}{T} = \frac{1}{T^2}\int \frac{(\epsilon-\mu)^2}{\cosh^2\left(\frac{\epsilon-\mu}{2T}\right)}\sigma_{xy}(\epsilon)d\epsilon \tag{4.56}$$

where μ is the chemical potential and $\sigma_{xy}(\epsilon)$ is the Hall coefficient for the system at zero temperature with chemical potential ϵ. We implement the linear-in-field approximation where calculation of κ_{xy} is greatly simplified at low magnetic field strengths[YZZ20], i.e. we write

$$\sigma_{xy}(\epsilon) \approx B\partial_B\sigma_{xy}(\epsilon)|_{B=0} = -B\tilde{\mathcal{B}}(\epsilon) \tag{4.57}$$

where B is magnitude of the magnetic field, and $\tilde{\mathcal{B}}(\epsilon)$ is the effective Berry curvature density given by

$$\tilde{\mathcal{B}}(\epsilon) = \sum_{nks}\mathcal{B}_{nsk}\delta(\epsilon-\epsilon_{nsk}). \tag{4.58}$$

Here $n=\pm1$ for the lower and upper bands, and the spin index $s=\pm1$. The Berry curvature and dispersion for the mixed triplet-singlet DDW are given by [HRC11]

$$\mathcal{B}_{nsk} = ns\frac{tW_0\Delta_0}{E_k^3}(\sin^2 k_y + \sin^2 k_x\cos^2 k_y), \tag{4.59}$$

$$\epsilon_{nsk} = \epsilon_{2k} - nE_k, \tag{4.60}$$

with E_k is defined as

$$E_k = \sqrt{4t^2(\cos k_x+\cos k_y)^2 + W_k^2 + \Delta_k^2}. \tag{4.61}$$

where

$$\begin{aligned} W_k &= \frac{W_0}{2}(\cos k_x - \cos k_y) \\ \Delta_k &= \Delta_0 \sin k_x \sin k_y, \end{aligned} \tag{4.62}$$

and

$$\epsilon_{2k} = 4t'\cos k_x\cos k_y. \tag{4.63}$$

Upon integration over ϵ, Eq. (4.56) simplifies to

$$\frac{\kappa_{xy}}{T} = \frac{B}{2T^3}\sum_{\substack{k\in RBZ\\ \alpha=\pm}}\mathcal{B}_{++k}\left[\frac{-\alpha(\epsilon_{\alpha\alpha k}-\mu)^2}{\cosh^2(\beta(\epsilon_{\alpha\alpha k}-\mu)/2)}\right] \tag{4.64}$$

which may be evaluated with ease. We numerically integrate this quantity and plot it in Fig. 4.1

REFERENCES

[ABA05] James G. Analytis, Stephen J. Blundell, and Arzhang Ardavan. "Magnetic oscillations, disorder and the Hofstadter butterfly in finite systems." *Synthetic Metals*, **154**(1):265–268, 2005. Proceedings of the International Conference on Science and Technology of Synthetic Metals.

[AC14] Vadim M. Apalkov and Tapash Chakraborty. "Gap Structure of the Hofstadter System of Interacting Dirac Fermions in Graphene." *Phys. Rev. Lett.*, **112**:176401, Apr 2014.

[ASK01] C. Albrecht, J. H. Smet, K. von Klitzing, D. Weiss, V. Umansky, and H. Schweizer. "Evidence of Hofstadter's Fractal Energy Spectrum in the Quantized Hall Conductance." *Phys. Rev. Lett.*, **86**:147–150, Jan 2001.

[CHN89] Sudip Chakravarty, Bertrand I. Halperin, and David R. Nelson. "Two-dimensional quantum Heisenberg antiferromagnet at low temperatures." *Phys. Rev. B*, **39**:2344–2371, Feb 1989.

[CK08] Sudip Chakravarty and Hae-Young Kee. "Fermi pockets and quantum oscillations of the Hall coefficient in high-temperature superconductors." *Proceedings of the National Academy of Sciences*, **105**(26):8835–8839, July 2008.

[CLM01] S Chakravarty, R B Laughlin, Dirk K Morr, and Chetan Nayak. "Hidden order in the cuprates." *Physical Review B*, **63**(9):116–10, January 2001.

[Col78] J H P Colpa. "Diagonalization of the quadratic boson hamiltonian." *Physica A: Statistical Mechanics and its Applications*, **93A**:327–353, September 1978.

[CRZ91] D Coffey, T M Rice, and F C Zhang. "Dzyaloshinskii-Moriya interaction in the cuprates." *Physical Review B*, **44**(18):10112–10116, November 1991.

[CTF89] S W Cheong, J D Thompson, and Z Fisk. "Metamagnetism in La_2CuO_4." *Physical Review B*, **39**(7):4395–4398, March 1989.

[CTV06] Davide Ceresoli, T Thonhauser, David Vanderbilt, and R Resta. "Orbital magnetization in crystalline solids: Multi-band insulators, Chern insulators, and metals." *Physical Review B*, **74**(2):024408–13, July 2006.

[DCL10] R Daou, J Chang, David LeBoeuf, Olivier Cyr-Choinière, Francis Laliberté, Nicolas Doiron-Leyraud, B J Ramshaw, Ruixing Liang, D A Bonn, W N Hardy, and Louis Taillefer. "Broken rotational symmetry in the pseudogap phase of a high-Tc superconductor." *Nature*, **463**(7280):519–522, 2010.

[DPL07] Nicolas Doiron-Leyraud, Cyril Proust, David LeBoeuf, Julien Levallois, Jean-Baptiste Bonnemaison, Ruixing Liang, D A Bonn, W N Hardy, and Louis Taillefer. "Quantum oscillations and the Fermi surface in an underdoped high-Tc superconductor." *Nature*, **447**(7144):565–568, May 2007.

[EM08] Ferdinand Evers and Alexander D. Mirlin. "Anderson transitions." *Rev. Mod. Phys.*, **80**:1355–1417, Oct 2008.

[FHS05] Takahiro Fukui, Yasuhiro Hatsugai, and Hiroshi Suzuki. "Chern Numbers in Discretized Brillouin Zone: Efficient Method of Computing (Spin) Hall Conductances." *Journal of the Physical Society of Japan*, **74**(6):1674–1677, June 2005.

[GG96] Vidar Gudmundsson and Rolf Gerhardts. "Is the Hofstadter energy spectrum observable in far-infrared absorption?" 09 1996.

[GLB19] G Grissonnanche, A Legros, S Badoux, E Lefrançois, V Zatko, M Lizaire, F Laliberté, A Gourgout, J S Zhou, S Pyon, T Takayama, H Takagi, S Ono, N Doiron-Leyraud, and L Taillefer. "Giant thermal Hall conductivity in the pseudogap phase of cuprate superconductors." *Nature*, **571**(7765):376–380, 2019.

[HF09] J T Haraldsen and R S Fishman. "Spin rotation technique for non-collinear magnetic systems: application to the generalized Villain model." *Journal of Physics: Condensed Matter*, **21**(21):216001–12, April 2009.

[HHK90] Y. Hasegawa, Y. Hatsugai, M. Kohmoto, and G. Montambaux. "Stabilization of flux states on two-dimensional lattices." *Phys. Rev. B*, **41**:9174–9182, May 1990.

[Hof76] Douglas R. Hofstadter. "Energy levels and wave functions of Bloch electrons in rational and irrational magnetic fields." *Phys. Rev. B*, **14**:2239–2249, Sep 1976.

[HPL19] Jung Hoon Han, Jin-Hong Park, and Patrick A Lee. "Consideration of thermal Hall effect in undoped cuprates." *Physical Review B*, **99**(20):1–10, May 2019.

[HRC11] Chen-Hsuan Hsu, S Raghu, and Sudip Chakravarty. "Topological density wave states of nonzero angular momentum." *Physical Review B*, **84**(15):155111–6, October 2011.

[JGC09] Xun Jia, Pallab Goswami, and Sudip Chakravarty. "Resolution of two apparent paradoxes concerning quantum oscillations in underdoped high-T_c superconductors." *Phys. Rev. B*, **80**:134503, Oct 2009.

[KGC07] Angela Kopp, Amit Ghosal, and Sudip Chakravarty. "Competing ferromagnetism in high-temperature copper oxide superconductors." *Proceedings of the National Academy of Sciences*, **104**(15):6123–6127, April 2007.

[KH19] Masataka Kawano and Chisa Hotta. "Thermal Hall effect and topological edge states in a square lattice antiferromagnet." *Physical Review B*, **99**(5):4422–1–4422–16, February 2019.

[KK03] A P Kampf and A A Katanin. "Competing phases in the extended U-V-J Hubbard model near the Van Hove fillings." *Physical Review B*, **67**(12):4126–14, March 2003.

[KKA16] Toru Kikuchi, Takashi Koretsune, Ryotaro Arita, and Gen Tatara. "Dzyaloshinskii-Moriya Interaction as a Consequence of a Doppler Shift due to Spin-Orbit-Induced Intrinsic Spin Current." *Physical Review Letters*, **116**(24):247201–6, June 2016.

[KKM10] M I Katsnelson, Y O Kvashnin, V V Mazurenko, and A I Lichtenstein. "Correlated band theory of spin and orbital contributions to Dzyaloshinskii-Moriya interactions." *Physical Review B*, **82**(10):100403–4, September 2010.

[Lau14] R B Laughlin. "Hartree-Fock computation of the high-Tc cuprate phase diagram." *Physical Review B*, **89**(3):035134–19, January 2014.

[LC15] Wenchen Luo and Tapash Chakraborty. "Excitation gap of fractal quantum hall states in graphene." *Journal of Physics: Condensed Matter*, **28**(1):015801, dec 2015.

[LL19] Zi-Xiang Li and Dung-Hai Lee. "The thermal Hall conductance of two doped symmetry-breaking topological insulators." *arXiv.org*, May 2019.

[MBZ04] S. Melinte, Mona Berciu, Chenggang Zhou, E. Tutuc, S. J. Papadakis, C. Harrison, E. P. De Poortere, Mingshaw Wu, P. M. Chaikin, M. Shayegan, R. N. Bhatt, and R. A. Register. "Laterally Modulated 2D Electron System in the Extreme Quantum Limit." *Phys. Rev. Lett.*, **92**:036802, Jan 2004.

[McC56] J.W. McClure. *Phys. Rev.*, **104**:666, 1956.

[MM11] Ryo Matsumoto and Shuichi Murakami. "Theoretical Prediction of a Rotating Magnon Wave Packet in Ferromagnets." *Physical Review Letters*, **106**(19):197202–4, May 2011.

[Mor60] Toru Moriya. "Anisotropic Superexchange Interaction and Weak Ferromagnetism." *Phys. Rev.*, **120**(1):91–98, October 1960.

[MSM14] Ryo Matsumoto, Ryuichi Shindou, and Shuichi Murakami. "Thermal Hall effect of magnons in magnets with dipolar interaction." *Physical Review B*, **89**(5):054420–12, February 2014.

[Nau16] Gerardo G. Naumis. "Topological map of the Hofstadter butterfly: Fine structure of Chern numbers and Van Hove singularities." *Physics Letters A*, **380**(20):1772–1780, 2016.

[Nay00a] Chetan Nayak. "Density-wave states of nonzero angular momentum." *Phys. Rev. B*, **62**:4880–4889, Aug 2000.

[Nay00b] Chetan Nayak. "Density-wave states of nonzero angular momentum." *Physical Review B*, **62**(8):4880–4889, August 2000.

[NJK99] A A Nersesyan, G I Japaridze, and I G Kimeridze. "Low-temperature magnetic properties of a two-dimensional spin nematic state." *Journal of Physics: Condensed Matter*, **3**(19):3353–3366, January 1999.

[NPK07] M R Norman, D Pines, and C Kallin. "The pseudogap: friend or foe of high Tc?" *Advances in Physics*, **54**(8):715–733, February 2007.

[Pei33] R. Peierls. "On the theory of diamagnetism of conduction electrons." *Z. Phys.*, **80**:763–791, 1933.

[PG92] Daniela Pfannkuche and Rolf R. Gerhardts. "Theory of magnetotransport in two-dimensional electron systems subjected to weak two-dimensional superlattice potentials." *Phys. Rev. B*, **46**:12606–12626, Nov 1992.

[QNS11] Tao Qin, Qian Niu, and Junren Shi. "Energy Magnetization and the Thermal Hall Effect." *Physical Review Letters*, **107**(23):236601–5, November 2011.

[QZS12] Tao Qin, Jianhui Zhou, and Junren Shi. "Berry curvature and the phonon Hall effect." *Physical Review B*, **86**(10):1913–9, September 2012.

[Ram85] R. Rammal. "On the theory of diamagnetism of conduction electrons." *J. Phys. (Paris)*, **46**, 1985.

[Sac11] Subir Sachdev. *Quantum Phase Transitions*. Cambridge University Press, 2 edition, 2011.

[Sch89] H J Schulz. "Fermi-surface instabilities of a generalized two-dimensional Hubbard model." *Physical Review B*, **39**(4):2940–2943, February 1989.

[SCS19] Rhine Samajdar, Shubhayu Chatterjee, Subir Sachdev, and Mathias S Scheurer. "Thermal Hall effect in square-lattice spin liquids: A Schwinger boson mean-field study." *Physical Review B*, **99**(16):165126, April 2019.

[SHP08] Suchitra E Sebastian, N Harrison, E Palm, T P Murphy, C H Mielke, Ruixing Liang, D A Bonn, W N Hardy, and G G Lonzarich. "A multi-component Fermi surface in the vortex state of an underdoped high-Tc superconductor." *Nature*, **454**(7201):200–203, July 2008.

[SMM13] Ryuichi Shindou, Ryo Matsumoto, Shuichi Murakami, and Jun-ichiro Ohe. "Topological chiral magnonic edge mode in a magnonic crystal." *Physical Review B*, **87**(17):174427–11, May 2013.

[SWZ20] Tarapada Sarkar, D S Wei, J Zhang, N R Poniatowski, P R Mandal, A Kapitulnik, and Richard L Greene. "Ferromagnetic order beyond the superconducting dome in a cuprate superconductor." *Science*, **368**(6490):532–534, May 2020.

[TA94] Tineke Thio and Amnon Aharony. "Weak Ferromagnetism and Tricriticality in Pure La_2CuO_4." *Physical Review Letters*, **73**(6):894–897, August 1994.

[Tat19] Gen Tatara. "Effective gauge field theory of spintronics." *Physica E: Low-dimensional Systems and Nanostructures*, **106**:208–238, February 2019.

[TKN82] D. J. Thouless, M. Kohmoto, M. P. Nightingale, and M. den Nijs. "Quantized Hall Conductance in a Two-Dimensional Periodic Potential." *Phys. Rev. Lett.*, **49**:405–408, Aug 1982.

[Var99] C M Varma. "Pseudogap Phase and the Quantum-Critical Point in Copper-Oxide Metals." *Physical Review Letters*, **83**(17):3538–3541, October 1999.

[Var06] C M Varma. "Theory of the pseudogap state of the cuprates." *Physical Review B*, **73**(15):53–17, April 2006.

[Wan78] G. H. Wannier. "A Result Not Dependent on Rationality for Bloch Electrons in a Magnetic Field." *Physica Status Solidi B Basic Research*, **88**(2):757–765, August 1978.

[WC16] Zhiqiang Wang and Sudip Chakravarty. "Onsager rule, quantum oscillation frequencies, and the density of states in the mixed-vortex state of cuprates." *Physical Review B*, **93**(18):184505, May 2016.

[WZ09] Jian-Sheng Wang and Lifa Zhang. "Phonon Hall thermal conductivity from the Green-Kubo formula." *Physical Review B*, **80**(1):012301–4, July 2009.

[XSD08] Jing Xia, Elizabeth Schemm, G Deutscher, S A Kivelson, D A Bonn, W N Hardy, R Liang, W Siemons, G Koster, M M Fejer, and A Kapitulnik. "Polar Kerr-Effect Measurements of the High-Temperature $YBa_2Cu_3O_{6+x}$ Superconductor: Evidence for Broken Symmetry near the Pseudogap Temperature." *Physical Review Letters*, **100**(12):127002–4, March 2008.

[Y 05] H. L. Stormer P. Kim Y. Zhang, Yan-Wen Tan. *Nature*, **438**:201–204, 2005.

[YJ18] S. Fang K. Watanabe T. Taniguchi E. Kaxiras Y. Cao, V. Fatemi and P. Jarillo-Herrero. "Hofstadter's butterfly and the fractal quantum Hall effect in moire superlattices." *Nature (London)*, **556**, 2018.

[YRZ06] Kai-Yu Yang, T M Rice, and Fu-Chun Zhang. "Phenomenological theory of the pseudogap state." *Physical Review B*, **73**(17):R755–10, May 2006.

[YZZ20] Yi-feng Yang, Guang-Ming Zhang, and Fu-Chun Zhang. "Universal Behavior of the Thermal Hall Conductivity." *Physical Review Letters*, **124**(18):186602, May 2020.

[ZBL16] L Zhao, C A Belvin, R Liang, D A Bonn, W N Hardy, N P Armitage, and D Hsieh. "A global inversion-symmetry-broken phase inside the pseudogap region of YBa2Cu3Oy." *Nature Physics*, **13**(3):250–254, November 2016.